



Highly active and durable chlorobenzene oxidation catalyst via porous atomic layer coating of Ru on Pt/Al₂O₃

Yu Wang^{a,d,1}, Chun Du^{b,1}, Zhang Liu^{a,b}, Yanfei Liu^b, Bin Shan^{b,*}, Limin Guo^{a,*}, Rong Chen^c

^a School of Environmental Science and Engineering, Huazhong University of Science and Technology, Wuhan 430074, PR China

^b State Key Laboratory of Materials Processing and Die and Mould Technology, School of Materials Science and Engineering, Huazhong University of Science and Technology, Wuhan 430074, PR China

^c State Key Laboratory of Digital Manufacturing Equipment and Technology, School of Mechanical Science and Engineering, Huazhong University of Science and Technology, Wuhan 430074, PR China

^d College of Resources and Environment Engineering, Wuhan University of Science and Technology, Wuhan 430081, PR China

ARTICLE INFO

Keywords:

Ruthenium

Platinum

ALD

CVOCs

Catalytic combustion

Subnanometer

ABSTRACT

Herein, we designed and fabricated a novel subnanometer Ru-coating Pt/Al₂O₃ catalyst (named RuPt-ALD) via atomic layer deposition (ALD), which showed an excellent capability of tuning catalysts' structure-property relationship for chlorobenzene (CB) oxidation. Subnanometer Ru clusters were separately decorated onto Pt nanoparticles, while leaving neighboring Pt surfaces exposed, which could effectively enhance the substrate-particles interaction by electron donation. RuPt-ALD provided optimal activity and selectivity, and a stable CB conversion of ~98 % for 600 min at 200 °C in humid air, superior to bare Ru or Pt samples. Experimental verification and theoretical calculation identified that the relative lower barriers of CB adsorption and O₂ dissociation on RuPt-ALD contributed to its stronger CB adsorption and appropriate oxygen activation capacity, which were the core factors for the excellent performance under humid feed. In addition, under dry feed, the desorption ability of Cl species was also a key factor affecting the performance of Pt-based catalysts.

1. Introduction

Air pollution is a global emergency claiming millions of lives every year that goes beyond national borders. Creating a green atmospheric environment has become one of the hot topics concerned by all walks of life. Chlorinated volatile organic compounds (CVOCs) exhaust gas purification is an important measure to control ozone, fine particulate matter (PM_{2.5}), photochemical smog, organic aerosol and to improve the quality of atmospheric environment [1,2]. So far, catalytic oxidation is considered to be the most effective and promising technology for CVOCs removal due to its high catalytic performance (i.e., activity, selectivity and stability), sound security and small occupation [3,4]. Research and development of highly active catalysts is the key to the development of this technique. Particularly, the catalysts should be resistant to deactivation at low-temperature operation by Cl species produced [5,6].

Recently, Wang and Guo et al. [7] found that a bimetallic Pt-Ru catalyst supported on hierarchical HZSM-5 zeolites prepared by an co-impregnation showed promoted catalytic activities for the

chlorobenzene (CB) oxidation reaction. Close agreement could be reached between the activity in CB oxidation and structural and chemical properties on the basis of the detailed experimental analysis. In addition, it was discovered that the well-characterized Pt-Ru bicomponent structure was demonstrated for CB oxidation. This structure improved the reducibility and acidity and showed high-resistance to Cl species. However, the detailed location of each metal site can hardly be controlled by the traditional wet-chemistry method such as co-impregnation and coprecipitation [8]. As a result, most Pt and Ru nanoparticles (NPs) were separately dispersed on the surface of zeolite, while only a small fraction of the precursors formed the Pt-Ru bimetal composite structure during the traditional co-impregnation [7]. Therefore, it remains a great challenge to synthesize high-quality Pt-Ru bimetallic structures with intimate contact to further enhance the activity toward CVOCs oxidation.

Atomic layer deposition (ALD) has emerged as a powerful tool to assemble controllable particle and engineer the interface [9]. Especially, ALD has recently found extensive application as a facile method of

* Corresponding authors.

E-mail addresses: bshan@mail.hust.edu.cn (B. Shan), lmguo@hust.edu.cn (L. Guo).

¹ Y. Wang and C. Du contribute equally to this manuscript.

bimetallic catalysts synthesis and enhancement through synergetic effects, such as Pt-coated Cu/CeO₂ [10], Ti-coated Pd/Al₂O₃ [11], Pt-coated TiO₂/GC [12] and Pt-coated Ru/Al₂O₃ [13], etc. Through precise control of the ALD deposition conditions, the second metal can be selectively deposited on the initial metal deposition sites, leading to the formation of intimate contacts between two components. For example, Sun and co-workers [14] successfully obtained Pt-Ru bimetallic structures by a two-step ALD process. The Pt-Ru dimers exhibited more than 50 times higher hydrogen evolution activity and excellent stability compared to commercial Pt/C catalysts. Recently, Shan and Chen et al. [13] designed and fabricated bifunctionally faceted Pt/Ru nanoparticle catalysts via selective ALD, which offered an unprecedented capability of tuning nanoparticles' structure-property relationship for preferential oxidation of CO in H₂. The source of the activity can be traced to the elimination of competitive CO adsorption on Pt where neighboring Ru sites provide highly active sites for O₂ dissociation. Obviously, ALD method can maximize the construction of Pt-Ru bimetallic structure through well controlled selective deposition strategy. It may not only improve the utilization of noble metals, but also significantly improve the catalytic performance because of the increase in the number of active sites.

Herein, we have designed an ALD route and fabricated the Ru-coated Pt dimers on γ -Al₂O₃. The as-prepared RuPt-ALD catalyst showed higher activity for CB oxidation than monometallic Pt or Ru samples. In detail, excellent catalytic activity with a T₅₀ and T₉₀ of 176 and 196 °C (167 ppm CB/humid air, GHSV = 20,000 h⁻¹), scarce formation of chlorinated byproduct (DCB) and good durability were obtained. The detailed material characterizations were carried out to prove the micro-structure and illustrate the active origins of RuPt-ALD catalyst. Density functional theory (DFT) calculation results indicated that the charge transfer between Pt atom and Ru cluster makes Ru atom effectively anchored. In addition, the adsorption and desorption ability of different samples to the reactants and products was also studied by DFT calculations.

2. Experimental

2.1. Catalyst preparation

Bare Pt and Ru catalysts were prepared by conventional incipient wetness impregnation method using water solution of hexachloroplatinic acid (Sinopharm Chemical Reagent Co., Ltd, AR), ruthenium trichloride (Aladdin, AR) and γ -Al₂O₃ (Aladdin, 99.99 %), followed by drying at 120 °C for 12 h and then calcined at 400 °C for 4 h in air. The obtained catalysts were denoted as Pt-IM and Ru-IM. The nominal metal loading of Pt-IM and Ru-IM were 2 wt% and 1 wt%, respectively. The element analysis results were obtained by ICP and listed in Table 1. The actual metal loading of Pt-IM and Ru-IM were measured as 1.65 wt% and 0.83 wt%, respectively.

For the Ru-coated Pt/ γ -Al₂O₃ sample, Ru was deposited on Pt-IM sample via atomic layer deposition (ALD, Picosun R-200). In the ALD process, Bis-(ethylcyclopentadienyl) ruthenium (Ru (Etcp)₂) was used as Ru precursor, and the growth temperature was set at 275 °C. In a typical Ru ALD process, the deposition was executed by the sequential exposure

of bis-(ethylcyclopentadienyl) ruthenium (Ru (Etcp)₂) and oxygen (O₂) with 50 ALD cycles. Each growth sequence consisted of 1.6 s Ru (Etcp)₂ and 3 s O₂, while a 10 s purge of N₂ (>99.99 %) was performed between Ru precursor pulse and oxygen pulse to eliminate the residual precursors. The obtained catalysts were denoted as RuPt-ALD. The actual Pt and Ru loading of RuPt-ALD were 1.61 wt% and 0.14 wt%, respectively (Table 1). Due to the lattice mismatch between the Ru and Pt facets, the deposited Ru forms a porous coating rather than uniform layer on Pt, exposing both Ru and Pt sites¹⁰. Notably, this work did not strictly optimize the Ru content, because the deposition rate of Ru in existing ALD process is slow, which is two orders of magnitude slower than Pt or Pd deposition. Even after 50 ALD cycles, the deposition amount of Ru is only 0.14 wt%, and higher Ru contents are currently difficult to achieve.

2.2. Catalyst characterization

The catalysts were characterized by means X-ray diffraction (XRD), N₂ adsorption-desorption (BET), transmission electron microscopy (TEM), inductively coupled plasma (ICP), X-ray photoelectron spectroscopy (XPS), H₂-temperature-programmed reduction (H₂-TPR), Temperature-programmed desorption of ammonia (NH₃-TPD), and CO Fourier transform infrared (CO-FTIR) experiments. Periodic DFT calculations with spin polarization were performed using the Vienna Ab Initio Simulation Package (VASP). The detailed characterization procedures and DFT calculations are described in the [Supporting information](#).

2.3. Catalytic activity measurement

Catalytic oxidation of CB was implemented in a miniature reactor with the measuring range at 80–320 °C in a quartz tube with 4 mm inner diameter. Gaseous H₂O was introduced into the gas stream by passing the simulated air (53 mL/min N₂ + 13 mL/min O₂) through a bubbler in a water bath, the water bath was kept at 33 °C, and the partial pressure of H₂O is approximately 5 vol%. CB liquid was delivered to the mixing humid air at the calculated rate by the syringe pump (KD scientific, KDS100). In addition, the injection site and the entire pipeline were covered with a heating strip to ensure that the reactants were completely vaporized. The intake condition was a mixed gas stream of 167 ppm CB/5 vol% H₂O/air, with a GHSV at 20,000 mL/g h at a flow rate of 66 mL/min, and the catalyst mass was 200 mg, and the rate of syringe pump was 3.0 μ L/h. The rate of the syringe pump (r) was calculated based on the equation below:

$$r = \frac{C_{CB} \times Q \times M_{CB}}{22.4 \times \rho_{CB}} \quad (1)$$

Where C_{CB} is the target CB concentration (167 ppm), Q is the flow rate (66 mL/min), M_{CB} is the relative molecular mass of CB (112.5 g/mol), 22.4 L/mol is the molar volume of gas, ρ_{CB} is the density of CB (1.1075 g/cm³), the calculated r value is 3.0 μ L/h. The catalyst was placed in the middle of quartz tube. The off-gases, including CB, DCB, CO and CO₂, were monitored online at different given temperatures by using a gas chromatograph (GC-9790II, FULI) equipped with FID, TCD

Table 1

ICP results, noble metal content and dispersion, BET surface area, pore volume and average pore size results of the as-prepared catalysts.

Catalysts	Pt ^a (wt%)	Ru ^a (wt%)	Ru or Pt diameter ^b (Å)	Dispersion ^c (%)	N ₂ sorption		
					S _{BET} (m ² /g)	P _V (cm ³ /g)	APD (nm)
γ -Al ₂ O ₃	-	-	-	-	137	0.16	5.6
Ru-IM	-	0.83	119	11.2	139	0.30	7.8
Pt-IM	1.65	-	28	40.4	137	0.28	7.7
RuPt-ALD	1.61	0.14	29	39.0	141	0.23	6.8

^a Determined by ICP-MS method.

^b By TEM. For RuPt-ALD, the Ru clusters deposited on the Pt surface were considered as a whole particle.

^c Dispersion of Ru or Pt was calculated by 6.66/ r and 5.66/ r , respectively, r is the radius (Å) of Ru or Pt.

and a nickel conversion furnace. The concentrations of Cl_2 were tested by the effluent stream bubbling through a 0.0125 M NaOH solution, and chlorine concentration was then determined by the titration with ferrous ammonium sulfate (FAS) using N,N-diethyl-p-phenylenediamine (DPD) as indicator, according to the references [15], and the detection limit of Cl_2 is 0.02 mg/L. The experimental error in conversion and selectivity were within $\pm 5\%$, respectively. Both external and internal diffusion limitations were excluded by varying the particle size of catalysts and W/F (the ratio of catalyst weight to the total flow rate). The CB conversion (X_{CB}) was calculated by Eq. (1):

$$X_{\text{CB}}(\%) = \frac{C_{\text{CB}}^{\text{in}} - C_{\text{CB}}^{\text{out}}}{C_{\text{CB}}^{\text{in}}} \times 100\% \quad (2)$$

where C^{in} and C^{out} are the inlet and outlet CB concentrations, respectively.

The CB conversion to CO, CO_2 , Cl_2 (denoted as S_{CO} , S_{CO_2} , and S_{Cl_2} , respectively) were calculated by Eqs. (2)–(5), respectively:

$$S_{\text{CO}}(\%) = \frac{C_{\text{CO}}^{\text{out}}}{6 \times C_{\text{CB}}^{\text{in}}} \times 100\% \quad (3)$$

$$S_{\text{CO}_2}(\%) = \frac{C_{\text{CO}_2}^{\text{out}}}{6 \times C_{\text{CB}}^{\text{in}}} \times 100\% \quad (4)$$

$$S_{\text{Cl}_2}(\%) = \frac{C_{\text{Cl}_2}^{\text{out}}}{0.5 \times C_{\text{CB}}^{\text{in}}} \times 100\% \quad (5)$$

where C_{CO} , C_{CO_2} , and C_{Cl_2} are the outlet CO, CO_2 , and Cl_2 concentrations, respectively.

3. Results and discussion

3.1. Phase compositions and textural properties of the catalysts

Fig. 1a performed the XRD patterns of $\gamma\text{-Al}_2\text{O}_3$ supported Ru-IM, Pt-IM and RuPt-ALD catalysts. For all Pt-contained samples, no apparent diffraction peaks of crystalline Pt or PtO_x suggested the high dispersion of Pt nanoparticles over the alumina framework. A slightly sharpness of Ru-IM peak at $2\theta = 28.1^\circ$, 35.2° and 54.4° was most likely related to the large RuO_2 crystallite size (PDF#40–1290). The crystallite size of RuO_2 was calculated using Scherrer equation at XRD peak of $2\theta = 28.1^\circ$, the value was 12.8 nm, which was close to that obtained from TEM image (average diameter of RuO_2 NPs was 11.9 nm, Table 1). To understand the reason that Pt is highly dispersed while Ru forms larger nanoparticles, it is proposed that the main difference results from the metal-support interaction (MSI). Pt tends to form very small nanoparticles on $\gamma\text{-Al}_2\text{O}_3$ with strong metal-support interaction (SMSI), similar conclusion has been reported in previous study [16]. However, for Ru impregnation, the property (e.g., morphology, valence state, or coordination number) of support (herein $\gamma\text{-Al}_2\text{O}_3$) is also very important. Recently, Peng et al. [17] reported a nano-flower sheet-like $\gamma\text{-Al}_2\text{O}_3$ sphere, which was beneficial for stabilizing Ru nanoparticles with rich unsaturated pentacoordinate Al^{3+} site. Ultrasmall size of Ru nanoparticles were observed in the TEM with average size of < 2 nm. However, in other reports, Abidin et al. [18] found the diffraction line of RuO_2 including 1 wt% Ru sample over $\gamma\text{-Al}_2\text{O}_3$ supports. Jeon et al. [19] also observed the XRD peaks due to RuO_2 over 1.5 wt% Ru/ $\gamma\text{-Al}_2\text{O}_3$ and Ru-MgO/ $\gamma\text{-Al}_2\text{O}_3$, and the crystallite size of Ru over the fresh Ru/ $\gamma\text{-Al}_2\text{O}_3$ was 32 nm based on Scherrer equation. Herein, the MSI between unpretreated commercial $\gamma\text{-Al}_2\text{O}_3$ and Ru is relatively weak, Ru nanoparticles may tend to aggregate and grow during drying and roasting processes. However, no peaks due to either Pt or Ru were detected over the RuPt-ALD sample suggesting the formation of highly dispersed nanoparticles or clusters. Another factor is the smaller content of Ru over RuPt-ALD (0.14 wt%) than that over Ru-IM (0.83 wt%).

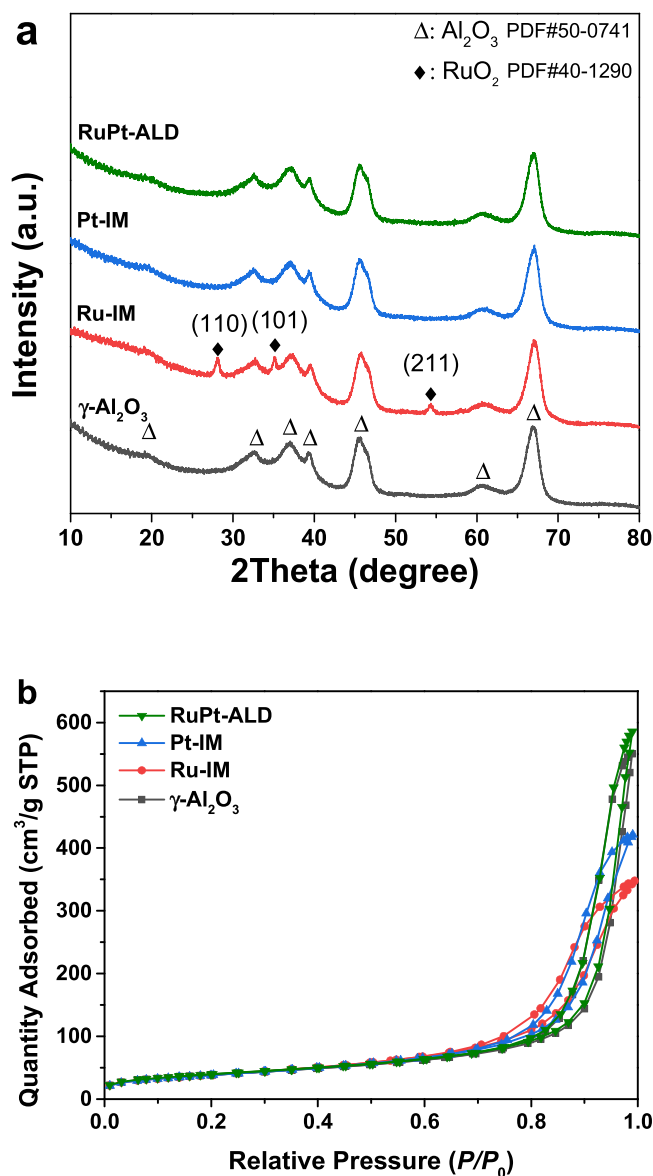


Fig. 1. (a) XRD patterns of the as-prepared catalysts. (b) N_2 sorption isotherms at -196°C of the as-prepared catalysts.

Nevertheless, XRD results indicate that the ALD technique may be an efficient method for the metal preparation with weak MSI with the support, such as the support of Ru on Al_2O_3 . This method may overcome the disadvantage of wet chemistry method and easier to prepare highly dispersed nanoparticles.

Fig. 1b exhibited the N_2 physisorption isotherms of the catalysts, while the corresponding textural properties of the samples were summarized in Table 1. The isotherms of the samples were quite similar. These samples exhibited type IV isotherms with hysteresis loop type H_2 for RuPt-ALD and $\gamma\text{-Al}_2\text{O}_3$ samples, whereas the Pt-IM and Ru-IM samples possessed the hysteresis loop type H_3 . Additionally, the BET surface area of these loaded samples was similar to the $\gamma\text{-Al}_2\text{O}_3$. However, a significant increase in the pore volume and average pore size of the loaded samples can be observed, which may be resulted from damage to the framework of $\gamma\text{-Al}_2\text{O}_3$. The increased mean pore diameter was most likely due to the pore destruction, creating larger pores and higher pore volume. In general, the destruction of framework of $\gamma\text{-Al}_2\text{O}_3$ may be due to the acidic precursor solution during noble metal impregnation. $\gamma\text{-Al}_2\text{O}_3$ could react with H^+ coming from the hydrolysis of precursor solution ($\text{Al}_2\text{O}_3 + 6\text{H}^+ = 2\text{Al}^{3+} + 3\text{H}_2\text{O}$), then resulted in the

enlargement of pores on γ - Al_2O_3 . A similar case was recently reported by Chen et al. [20], they found the mesoporous structure of $\text{Ru}/\gamma\text{-Al}_2\text{O}_3$ was affected by Cs impregnation, appearing to collapse based on N_2 adsorption-desorption isotherms. And they believed the crystalline framework of $\gamma\text{-Al}_2\text{O}_3$ was affected by the impregnation of basic Cs solutions ($\text{pH} = 11.0\text{--}12.5$). Moreover, the average pore size of Cs-Ru/ $\gamma\text{-Al}_2\text{O}_3$ (5.8 nm) was enlarged than original Ru/ $\gamma\text{-Al}_2\text{O}_3$ (5.4 nm), which is in good agreement with our conclusion (from 5.61 nm of $\gamma\text{-Al}_2\text{O}_3$ to 7.78 nm of Ru-IM, 7.73 nm of Pt-IM and 6.79 nm of RuPt-ALD, Table 1). In sum, acidic or alkaline solutions may react with $\gamma\text{-Al}_2\text{O}_3$ during the impregnation process to dissolve its pore structure. These larger P_v and APD were desirable for a higher mass transfer coefficient for enhanced catalytic performance. Note that the enlargement of pore size is an accidental result in the impregnation process. This accidental factor has a positive effect on CB catalytic oxidation reaction, but it is not the decisive factor.

The presence of metallic phases on the Ru-IM, Pt-IM and RuPt-ALD catalysts was revealed by STEM. Fig. 2a and b showed the micrograph of Ru-IM catalyst that indicated the presence of individual particles with clear lattice fringes. The high resolution TEM image of Ru-IM (Fig. 2b)

illustrated that the lattice fringes had interplanar distances of 2.54 Å, in agreement with the RuO_2 (101) planes, which strongly corroborated the XRD data. Fast Fourier transform (FFT) was used to estimate the lattice spacing of the crystallite. The FFT image (Fig. 2c) showed the lattice spacings of 0.13 and 0.17 nm that correspond to the (202) and (211) reflection planes of RuO_2 , respectively. Fig. 2d and e displayed STEM micrographs of Pt-IM and depicted the particles dispersion and lattice fringes. Pt NPs deposition at substrate resulted in a uniform nanoparticles distribution. The corresponding histogram of particle size distribution obtained by calculating about 200 particles revealed that the average particle size was about 2.8 nm for Pt-IM (Fig. S1a). As shown in Fig. 2e, the lattice plane with spacings of 2.03 Å corresponded to the (200) plane of Pt. FFT was also applied to this zone to assess the lattice spacing and compare to the d -spacing of the possible phases in the PDF cards. The FFT result in Fig. 2f matched the (111), (200), (311) and (222) reflection planes of the Pt crystallite. After ALD growth of Ru, Fig. S1b showed the STEM image of the RuPt-ALD catalyst. The size distribution of Ru-Pt particles (average size 2.9 nm) was similar to the Pt particle size in the Pt-IM catalyst, which was much smaller than the average size of RuO_2 over Ru-IM (11.9 nm, the size distribution was

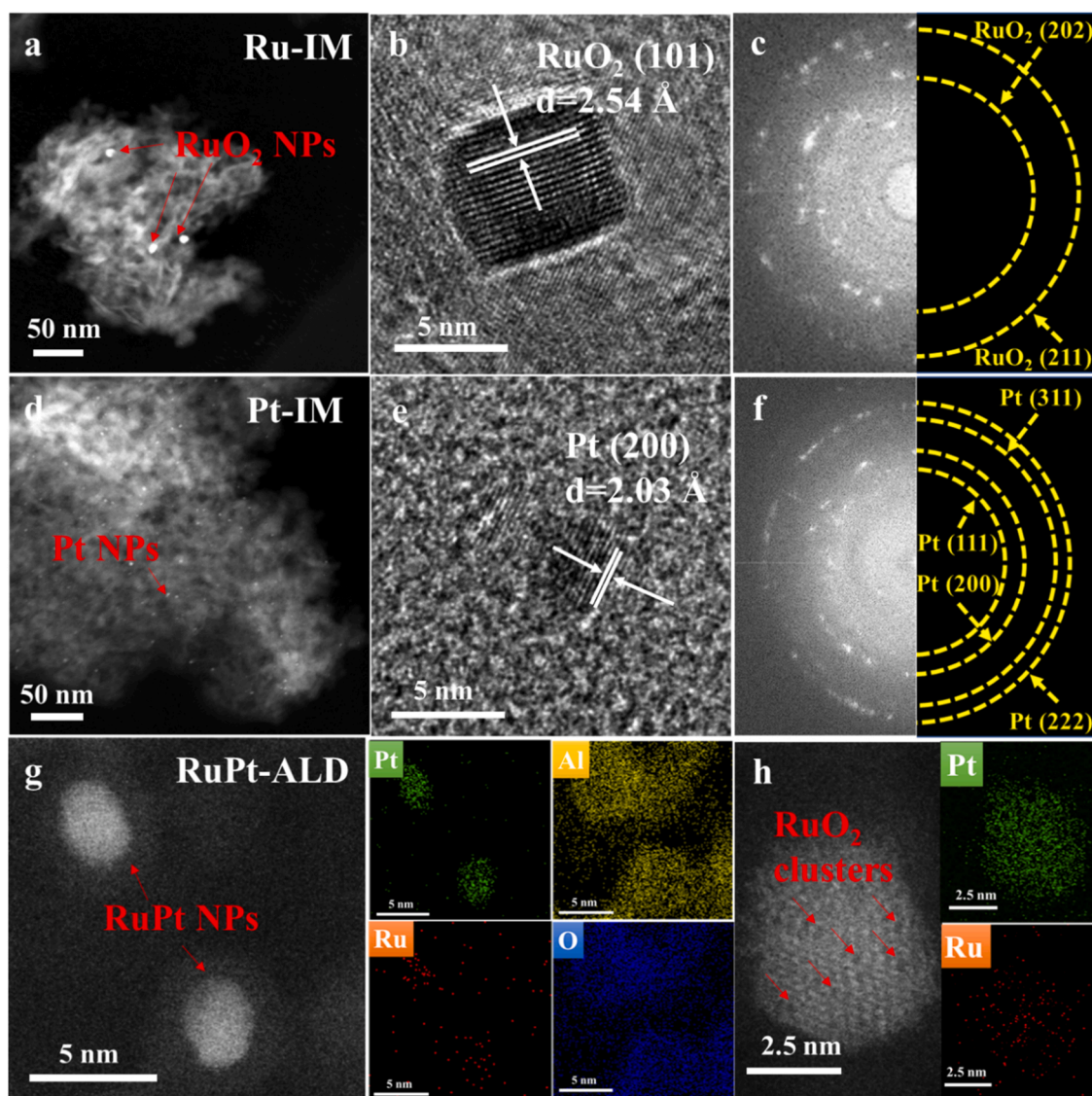


Fig. 2. The STEM images for (a,b) Ru-IM, (c) FFT patterns of the selected area electronic diffraction in (b). The STEM images for (d,e) Pt-IM, (f) FFT patterns of the selected area electronic diffraction in (e). STEM images for (g,h) RuPt-ALD and EDS elemental mapping of the same region of (g, h), indicating spatial distribution of Pt (green), Ru (red), O (blue) and Al (yellow).

shown in Fig. S1c). Based on TEM observations, we calculated the dispersion of noble metals in Table 1. Notably, subnanometric Ru or RuO₂ clusters was observed on Pt NPs, while no growth was observed on the Al₂O₃ support (Fig. 2g and h) [13]. STEM elemental maps of Pt, Al, Ru, and O of RuPt-ALD catalyst further demonstrated the phase distribution, confirming the Ru distribution over the surface of Pt NPs partially. This proves that coalescence of clusters occurs during Ru ALD, pointing towards a homogeneous growth of Ru clusters on Pt NPs. Such a growth mode is typical for a system with strong substrate-cluster interaction [21]. This idea has been proposed recently, Sun et al. [14] observed by the atomic resolution HAADF-STEM images that a dimer-like structure was successfully prepared by a two-step ALD process. The different contrast of the two atoms reflects that the dimer is composed of Pt and Ru.

3.2. Chemical properties of the catalysts

The adsorption strength and adsorption type of CO on Pt and Ru species were further analyzed by CO-desorption in situ FTIR experiments (Fig. 3a). For Pt-IM and RuPt-ALD samples, the CO adsorption led to an intense band centered around 2070 cm⁻¹, assigned to carbonyl species linearly adsorbed over Pt metal centers (Pt⁰-CO species). The frequency of RuPt-ALD (2068 cm⁻¹) was lower than that of Pt-IM (2074 cm⁻¹), suggesting that the oxidation state of Pt decreased after Ru coating. Besides, there was no CO linear adsorption of Ru species on Ru-IM sample. The lower wavenumbers at which the carbonyl band appeared reflected the higher electron density over Pt metal and

partially oxidized Ru sites. The band observed at 1848 cm⁻¹ was due to bridged Pt⁰-CO species for Pt-IM. The bands at 1915, 1835, and 1790 cm⁻¹ were located in a region attributing to CO anchored to two Ru sites bridge configuration (Ru^{δ+}-CO species) based on literature [22], which were produced by the oxidative disruption of very small Ru clusters. For the RuPt-ALD catalyst, the linear adsorption of CO on Pt NPs was enhanced (the band strength at 2068 cm⁻¹ became stronger), while the adsorption of CO at Pt-Pt bridge site decreased (the broad band at 1848 cm⁻¹ almost disappeared), and CO was mainly adsorbed in a bridged adsorption way on Ru surface (as seen the bands at 1915, 1835, and 1790 cm⁻¹). This phenomenon can be attributed to the replacement (or cover) by Ru atoms in the Pt lattice in the bridge adsorption planes, which is consistent with TEM observations. To further check the specific crystal planes, peak fitting was performed for the CO linearly adsorbed on Pt⁰ species, and the adsorption of CO on different Pt crystal planes was distinguished as shown in Fig. S2. Obviously, the main linear adsorption of CO on Pt-IM changes from Pt(111) to Pt(100) crystal planes on RuPt-ALD. This result indicates that the subnanometer Ru particles may prefer to deposit on the Pt(111) crystal plane and probably replaced some Pt atoms in the lattice.

XPS was performed to study the chemical composition and valence state of the catalysts in the composite. Fig. 3b showed the XPS spectra of Ru 3d and Pt 4d. Since the XPS spectra of C 1s and Ru 3d are overlapped with each other in the range of 284–279 eV, the spectra in this range were deconvoluted. For Ru-IM catalyst, the peaks at 280.0 and 280.8 eV can be assigned to Ru 3d_{5/2} core level, which were consistent with binding energies for of Ru⁰ and Ru⁴⁺ cations in RuO₂, respectively. On

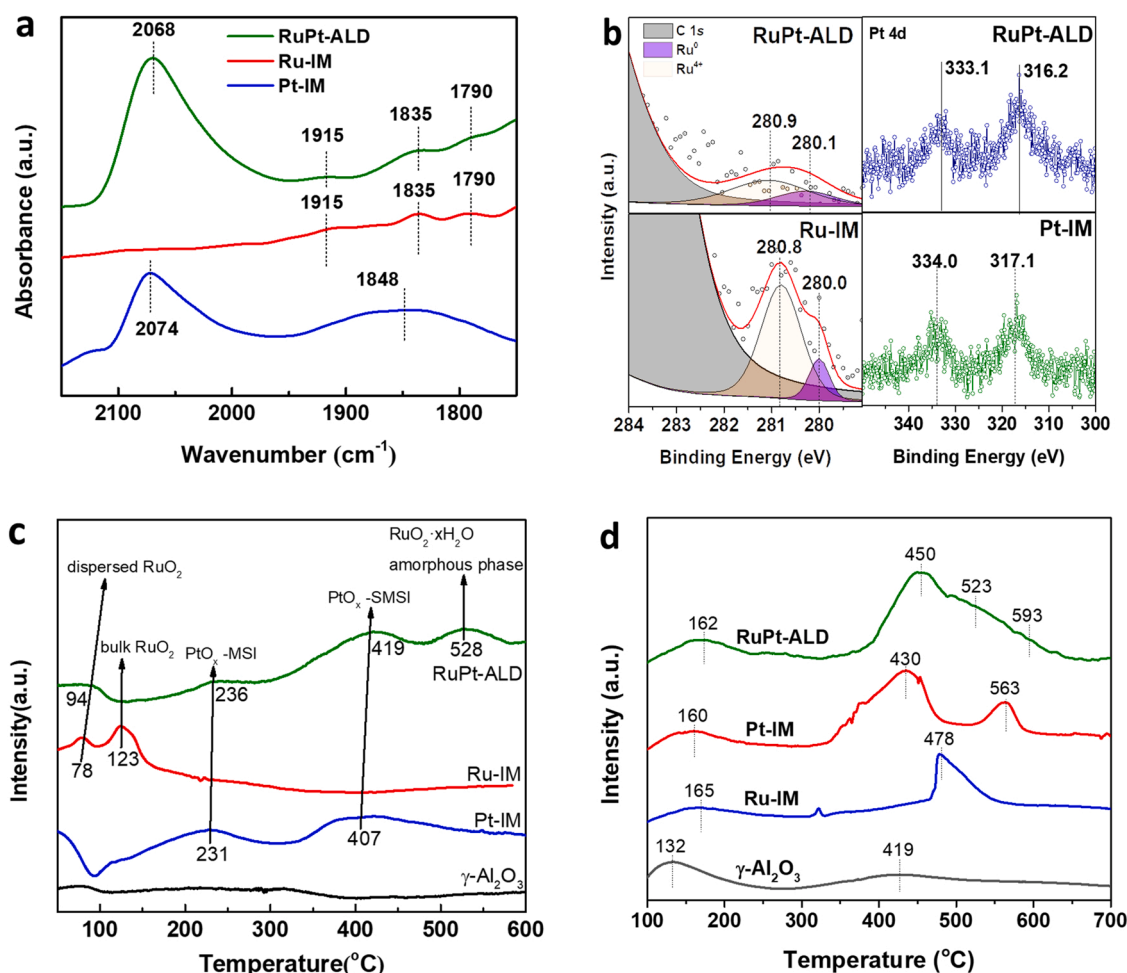


Fig. 3. (a) CO-FTIR spectrum of Ru-IM, Pt-IM and RuPt-ALD catalysts. (b) Ru 3d and Pt 4d XPS spectra of the Ru-IM, Pt-IM and RuPt-ALD catalysts. (c) H₂-TPR profiles of the catalysts and (d) NH₃-TPD profiles of the catalysts.

the opposite, for RuPt-ALD sample, the peak attributed to Ru^{4+} cations became much weaker, and the surface $\text{Ru}^0/\text{Ru}^{4+}$ molar ratio increased to its metal state. The variation in the Ru oxidation state can be explained by charge transfer from the underlying Pt NPs substrate, which is suggestive that smaller Ru atoms have incorporated into Pt lattices [23]. Although the most intense photoemission lines of Pt were Pt 4f, this energy region was seriously overlapped by the presence of a very strong Al 2p peak in this work, and thus the Pt 4d XPS spectrum were analyzed. The Pt-IM has the Pt 4d_{5/2} and Pt 4d_{3/2} peaks at around 317.1 and 334.0 eV, ascribing to a mixed phase between the substrate (Al_2O_3) and the PtO_x species, in which the chemical nature of the phase produced a more oxidized metal corresponding to ionic Pt^{2+} , Pt^{4+} and metallic Pt^0 [24]. For the RuPt-ALD sample, the binding energy of Pt 4d appeared around 316.2 and 333.1 eV, which shifted considerably lower than Pt-IM sample, suggesting a decrease of Pt oxidation state induced by the presence of Ru clusters, in agreement with the findings of CO-FTIR in Fig. 3a. This Pt 4d negative shift demonstrated that Pt atoms can obtain electrons from Ru atoms and result in a decrease in the d-band vacancy of Pt. A similar XPS result had been reported previously by Hoffmann et al. [25], who observed that the top surface of the SnO_2 layer is reduced to metallic Sn during the deposition of Pd particles, which facilitated the ALD process of Pd.

Reducibility of the as-prepared catalysts was measured by H_2 -TPR as shown in Fig. 3c, and the total H_2 consumption was calculated in Table 2. Bulk reduction of alumina was reported to occur above 600 °C [26], in essence outside the window of observation. Pt-IM catalyst presented two obvious reduction peaks located at 231 and 407 °C, respectively. Among them, the reduction peak around 231 °C was attributed to the reduction of PtO_x -MSI species that weakly interacted with Al_2O_3 , whereas the higher one was due to the reduction of PtO_x -SMSI species [27]. Ru-IM catalyst exhibited two major reduction peaks at 78 and 123 °C, both were caused by the reduction of RuO_2 to Ru^0 species but with different strengths of interaction with Al_2O_3 . The former can be assigned to the well-dispersed RuO_2 species and the latter was usually classified as the aggregated RuO_2 species [28]. Compared with bare Ru, the incorporation of Ru into Pt NPs via an ALD routine eliminated the bulk RuO_2 species, as evidenced by the disappearance of reduction peak around 123 °C over RuPt-ALD catalyst, which is consistent with TEM observations. Similar conclusion has also been reported in other literature, that ALD enabled the formation of Ru nanoparticles or clusters with uniform dispersion on the substrate and prevented aggregation [29]. Besides, the reduction peak located at 528 °C can be associated with a new formed Ru amorphous phase. It is proposed that this peak belongs to the reduction of oxygen species remote from $\text{RuO}_2 \cdot x\text{H}_2\text{O}$ species [30]. Notably, the reduction of Pt-IM began even below the sampling temperature. Clearly, there was a half-peak at 50 °C over Pt-IM, however, the redox capacity of Pt may be inhibited to some extent by the deposition of Ru over RuPt-ALD, thus the half-peak disappeared. Moreover, RuPt-ALD showed obvious shift for the reduction peaks of all species, including dispersed RuO_2 species (from 78 to 94 °C), PtO_x -MSI species (from 231 to 236 °C) and PtO_x -SMSI species (from 407 to 419 °C). The H_2 -TPR phenomenon manifested that a higher reduction temperature was needed to reduce the RuO_2 and PtO_x phases than when they are alone, indicating a strong interaction between Ru and Pt species due to

the ALD process. Notably, the strong redox property prefers multi-chlorine byproduct formation, which is unfavorable for the complete elimination of CB or other CVOCs [31].

Fig. 3d depicted the NH_3 -TPD profiles to investigate the surface acid sites amount and acidity strength distribution. Clearly, two primary peaks centered at 132 and 419 °C of the bare Al_2O_3 sample. The presence of low-temperature peak can be attributed to weak acid sites of Al_2O_3 support mainly to Lewis acid sites [32], where the high-temperature peak was ascribed to desorption of NH_3 from strong acid sites (from both Brønsted and Lewis acid). Pt-IM and Ru-IM samples exhibited intense desorption peaks of NH_3 from 400 to 600 °C, indicating the presence of stronger acid sites over the samples. These peaks were due to moderate or strong adsorbed ammonia on Lewis acid sites, and in particular, coordinatively unsaturated Pt and Ru atoms had an electron-accepting ability to adsorb ammonia molecules, which created new Lewis acid sites [7]. Suvanto and Pakkanen et al. [33] also reported that the Pt or PtO_x species on the surface would affect the acidity and were primarily related to the state of Pt on the surface of support (SiO_2 - Al_2O_3) and the metal-support interaction. In case of RuPt-ALD catalyst, the overlapping peak can be divided into three peaks at different temperature regions (450, 523 and 593 °C), which represent the moderate and strong acidic sites of ammonia desorption from Pt and Ru species. The acid amounts were also calculated using the NH_3 desorption peak areas (Table 2). Compared to the γ - Al_2O_3 (345 $\mu\text{mol/g}$), Ru-IM, Pt-IM and RuPt-ALD samples boasted higher amount of total acid sites (606, 779, and 904 $\mu\text{mol/g}$, respectively). Especially, for the moderate and strong acidic sites, Ru-IM, Pt-IM and RuPt-ALD catalysts increased to 469, 649 and 738 $\mu\text{mol/g}$, which verified that the incorporation of Ru and Pt could promote the formation of Lewis acid on the catalyst surface. Since the acid sites were reported to be crucial for dechlorination reaction and C-C bond cleavage [34]. The enhancement of Lewis acid can inhibit the accumulations of Cl, which further significantly suppress the formation of polychlorinated by-products such as dichlorobenzene (DCB). Moreover, the appropriate redox property and moderate/strong acid sites can reduce coke on catalyst surface and promote stability in CB oxidation [35]. Combined with the catalytic activities in Fig. 4, the amount of moderate and strong acid sites could be controlled by ALD doping, and the activity of CB oxidation was positively correlated with the quantity of moderate and strong acid sites.

3.3. Activity, stability and product selectivity for CB oxidation

Fig. 4a showed the catalytic performance of CB catalytic oxidation in simulated humid air over the as-prepared catalysts. In order to check whether some reactions under thermal oxidation condition could take place, blank test was carried out by pristine γ - Al_2O_3 packed in the reactor. As a result, no conversion was obtained below 260 °C and the conversion reached only about 5% even at 300 °C. Obviously, RuPt-ALD ($T_{50} = 176$ °C, $T_{90} = 196$ °C) revealed the best catalytic performance, which were remarkable lower than those of the monometallic Ru ($T_{50} = 248$ °C, $T_{90} = 274$ °C) and Pt ($T_{50} = 229$ °C, $T_{90} = 261$ °C) samples. This result indicated that the engineering of bimetallic site had induced a synergistic promotion in CB removal. According to the characterization results discussed above, the strong synergism between Pt and Ru

Table 2
XPS results, hydrogen consumption and acid sites of the as-prepared catalysts.

Catalysts	Pt (eV)		Ru (eV)		Total H_2 consumption ^a ($\mu\text{mol/g}$)	Acid sites ^b ($\mu\text{mol/g}$)		
	4d _{5/2}	4d _{3/2}	Ru (0)	Ru (IV)		Total NH_3 consumption	Weak (100–200 °C)	Moderate and strong (400–600 °C)
γ - Al_2O_3	-	-	-	-	-	345	131	214
Ru-IM	-	-	280.0	280.9	454	606	137	469
Pt-IM	317.1	334.0	-	-	255	779	130	649
RuPt-ALD	316.2	333.1	280.1	280.8	737	904	166	738

^a Data were estimated by quantitatively analyzing the H_2 -TPR profiles normalized by peak areas.

^b Data were estimated by quantitatively analyzing the NH_3 -TPD profiles normalized by peak areas.

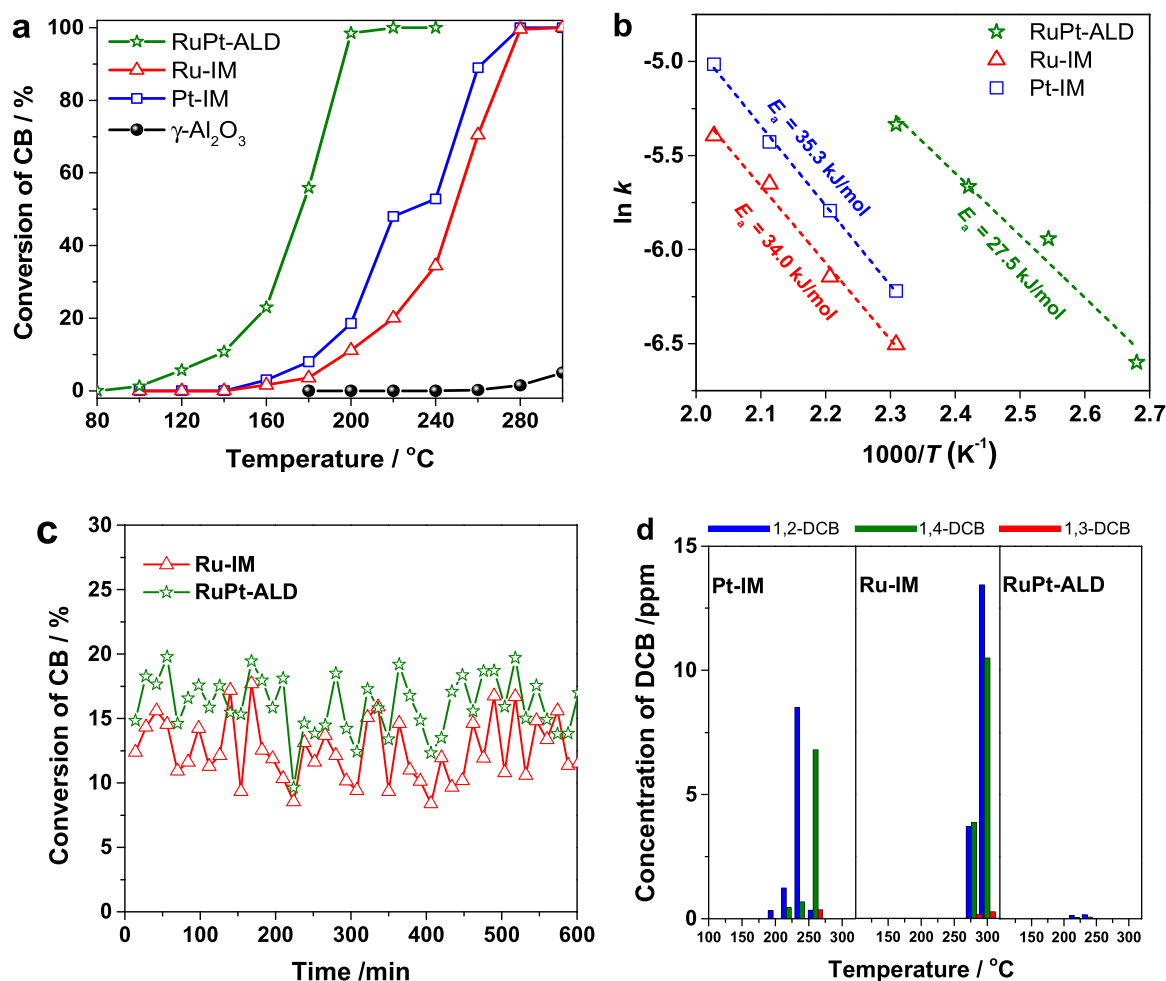


Fig. 4. (a) CB conversion as a function of temperature, (b) $\ln k$ versus inverse temperature, (c) stability data of CB oxidation tested at 200 °C, and (d) distribution of DCB by-products in function of temperature over the catalysts. Reaction condition: 167 ppm CB/5 vol% H₂O/air, GHSV = 20,000 mL/g h, catalyst mass: 200 mg.

enhanced Lewis acid and inhibit the accumulations of Cl. The deactivation of chlorine deposition on catalyst surface was inhibited over RuPt-ALD. On the contrary, a step appeared at 220–240 °C for Pt-IM catalyst, suggesting that Cl species may be gradually accumulated on Pt and covered the active sites, leading to the temporary deactivation and the presence of a step [36,37]. The Ru-IM catalyst appeared to be hardly affected by Cl poisoning in CB oxidation, because Ru⁴⁺ was also widely recognized as an active component for Cl species removal and total oxidation of CB [7,36,38,39]. As shown in Table 3, the reaction rate and TOF of RuPt-ALD were higher than Ru-IM and Pt-IM at 200 °C. Such as the TOF value ($75.3 \times 10^{-3} \text{ s}^{-1}$) of RuPt-ALD increased by about three and six times as those ($29.7 \times 10^{-3} \text{ s}^{-1}$ and $13.3 \times 10^{-3} \text{ s}^{-1}$) of Ru-IM and Pt-IM toward CB oxidation, respectively.

Over the past decade, CB oxidation was extremely studied and the activity data in the literature are shown in Table S1. Among the noble

metal catalysts, RuPt-ALD catalyst showed the lowest T_{90} (196 °C). Besides, we also calculated the reaction rates (v_{total}) normalized to per gram of total noble metal used. The v_{total} of RuPt-ALD catalyst at 200 °C was $8.35 \text{ mmol}/(\text{g}_{\text{noble}} \text{ h})$, which was comparable with the multifarious materials reported in the literatures, and significantly higher than that of Ru/SnO₂ ($2.21 \text{ mmol}/(\text{g}_{\text{noble}} \text{ h})$) [40], that of 1%Ru/TiO₂ ($1.34 \text{ mmol}/(\text{g}_{\text{noble}} \text{ h})$) [37], that of Ru5/Ti-350 ($3.33 \text{ mmol}/(\text{g}_{\text{noble}} \text{ h})$) [41], that of 1%Ru/SBA-15 ($0.59 \text{ mmol}/(\text{g}_{\text{noble}} \text{ h})$) [42], that of 1.5Pt/CeZr ($1.79 \text{ mmol}/(\text{g}_{\text{noble}} \text{ h})$) [43], and that of 2 wt%Pt/ γ -Al₂O₃ ($2.23 \text{ mmol}/(\text{g}_{\text{noble}} \text{ h})$) [44]. Apparent activation energy (E_a) value is a helpful tool to evaluate the catalytic performance. Herein, it was assuming that CB oxidation in the presence of 20 vol% oxygen would obey a first-order reaction mechanism with respect to CB concentration [45,46]. Fig. 4b showed the Arrhenius plots for the oxidation of CB over RuPt-ALD, Pt-IM, and Ru-IM. Note that for Ru-IM and RuPt-ALD

Table 3

Comparison of catalytic activities of CB oxidation in dry gas and humid gas.

Catalysts	Dry gas					Humid gas				
	T_{50} (°C)	T_{90} (°C)	v^a (mmol/(g h))	TOFs ^b (10^{-3} s^{-1})	E_a (kJ/mol)	T_{50} (°C)	T_{90} (°C)	v (mmol/(g h))	TOFs (10^{-3} s^{-1})	E_a (kJ/mol)
Ru-IM	223	238	4.03	60.5	41.3	245	274	1.98	29.7	34.0
Pt-IM	227	285	2.59	20.8	14.6	230	263	1.66	13.3	35.3
RuPt-ALD	143	167	8.43	76.3	25.0	176	196	8.31	75.3	27.5

^a The reaction rates (v) values were measured at 200 °C in kinetically controlled regime and normalized to per gram of noble metal used, note that for RuPt-ALD, the reaction rate and TOF value were calculated based on only Pt content and dispersion, the Ru cluster was not counted in.

^b The TOFs values were measured at 200 °C in kinetically controlled regime.

samples, their catalytic activities were stable at each test temperature, so the data were steady-state values. The Arrhenius plots for the rates of Ru-IM and RuPt-ALD were tested in kinetically controlled regime at their conversion < 25 % (at which the reaction temperature range was 160–220 and 100–160 °C), respectively. For Pt-IM sample, we tested the sample four times at 160, 180, 200 and 220 °C, respectively. Since the activity of the sample continued to decrease, but approximately leveled off after 60 min, we chose the conversion at 60 min to calculate the reaction rate at this temperature, as shown in Fig. S3. The activation energy is the minimum energy required to overcome the potential barrier to start the reaction. In a thermal catalytic oxidation reaction, the energy of the reactant molecule is expressed as the reaction temperature. The activation energy reflects the influence of temperature on the reaction rate. When the activation energy is higher, the influence of temperature is larger. The results showed that RuPt-ALD had the lowest activation energy value (27.5 kJ/mol, Table 3), suggesting that CB was easier to activate on the RuPt-ALD, which is consistent with the activity tests.

The durability test of RuPt-ALD and Ru-IM was conducted at GHSV of 132,000 mL/g h and 20,000 mL/g h, respectively, and 167 ppm CB/humid air at 200 °C. The CB conversion was studied as a function of time from 0 to 600 min, as revealed in Fig. 4c. No remarkable change was observed over RuPt-ALD and Ru-IM catalysts for the catalytic performances during 600 min at 200 °C. These catalysts showed efficient stabilities and achieved CB conversion of approximately 15% and 12%, respectively. The results confirmed that the activity of Ru-based catalysts could be maintained as the fresh catalyst. In contrast, CB conversion over Pt-IM was unstable as shown in Fig. S3. These contrasting results implied that the stability of RuPt-ALD catalyst strongly depended on the existence of Ru. RuPt-ALD with stronger resistance to chlorine poisoning and oxygen activation capacity was more catalytically stable. On the contrary, the deactivation reason of Pt-based catalysts was more complicated. In dry feed, Pt/Al₂O₃ would deactivate easily in CVOC oxidation due to Cl strong adsorption. Wang et al. [47] observed that Pt/TiO₂ was easily deactivated and showed the poorest performance for dichloromethane (CH₂Cl₂) decomposition under 1000 ppm CH₂Cl₂/10 % O₂/balance N₂. Deactivation of the catalysts was related to the deposition of carbon species and chlorine poisoning, whereby the active sites for DCM decomposition were occluded. For Pt/CeO₂ catalyst, similarly, the low activity for CVOC oxidation in dry feed really resulted from strong Cl adsorption on CeO₂ and Pt surface [48]. However, the activity of Pt/CeO₂ in wet feed is almost unchanged as that in dry feed, indicating that Pt species would interact with benzene rings to form π -complexes [48]. Therefore, the deactivation of Pt-IM sample in wet feed may be due to CB adsorption on the Pt site by π -complexation, this strong adsorption may lead to carbon deposition inactivation of Pt-IM. Other possibilities are the modification of Pt structure in the presence of water, such as the exposed crystal surface, valence and/or particle size of Pt NPs. Besides, some studies have found that in wet feed, Cl removal was promoted greatly, thus promoting the CB oxidation of Pt/Al₂O₃ catalyst [44].

Studies of product selectivity were shown in Fig. S4a, CO₂ was the major oxidation product in CB oxidation over the as-prepared catalysts (carbon balance ≥ 99.5 %). In Fig. S4b, no Cl₂ was produced in the catalytic process over Pt-IM and RuPt-IM. Cl₂ was detected at higher than 240 °C over Ru-IM, probably because Ru was highly reactive to Deacon reaction ($2\text{HCl} + 1/2 \text{O}_2 \rightarrow \text{H}_2\text{O} + \text{Cl}_2$), which inevitably generated Cl₂ in the presence of O₂ [49]. For the products of CB chlorination, DCB were also detected (Fig. 4d). The production of DCB isomers were mainly 1,2-DCB and 1,4-DCB, which is in agreement with literatures [50,51]. Notably, the yield of DCB was much higher for the Pt-IM and Ru-IM catalysts than for the RuPt-ALD. Almost no by-product formation was observed on RuPt-ALD sample. As is known, the formation of DCB could be attributed to chlorination of CB by Cl species (especially Cl₂) through an aromatic electrophilic substitution mechanism ($2\text{CB} + \text{Cl}_2 \rightarrow 1,2\text{-DCB} + 1,4\text{-DCB}$). And the partially chlorinated

RuO_xCl_y or PtO_xCl_y acted as Lewis acid catalysts driven the production of DCB. Apparently, the lowest amount of DCB over RuPt-ALD is beneficial from the following three factors: (1) the complete conversion temperature is ca. 200 °C, much lower than the temperature at which Deacon reaction takes place (normally > 240 °C); (2) the production rate of DCB is slow due to the lack of RuO_xCl_y or PtO_xCl_y as Lewis acid catalysts; (3) most of DCB formed during the reaction can be converted, due to the occurrence of chlorination at a significantly high temperature, in other words, the smaller amount of DCB over RuPt-ALD is related to its higher activity for CB oxidation.

3.4. Comparison of spent and fresh catalysts

To understand the redox and acid ability changes after the catalytic reaction, the spent and fresh RuPt-ALD catalysts were characterized by H₂-TPR and NH₃-TPD as shown in Fig. 5a and b, respectively. Overall, there was no significant change in the redox and acid ability of the RuPt-ALD-spent sample, which proved its great catalytic stability. The PtO_x

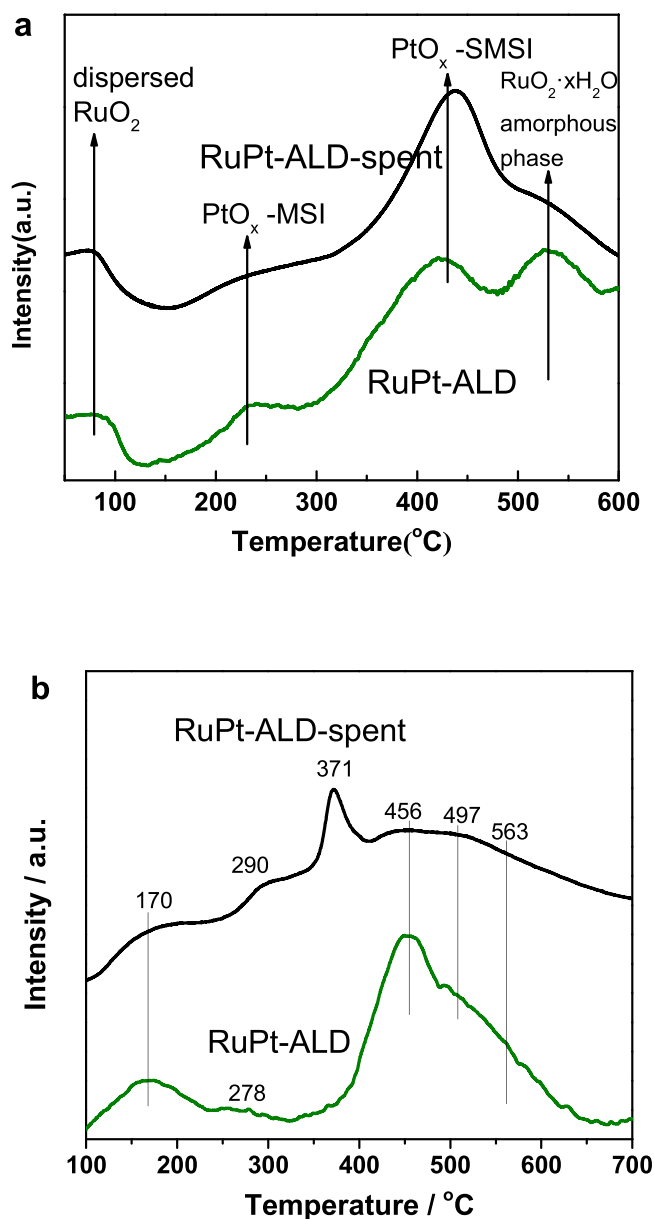


Fig. 5. (a) H₂-TPR and (b) NH₃-TPD profiles of the fresh and spent RuPt-ALD catalysts.

reduction peak between 200 and 250 °C decreased slightly, probably due to some of the chemisorbed oxygen located at oxygen vacancies and surface lattice oxygen of PtO_x and O in the Pt-O-Ru interface were consumed. A small NH_3 desorption peak at 371 °C was observed, may be due to part of the Ru and/or Pt NPs were chloridized by Cl ions by forming RuO_xCl_y or PtO_xCl_y as new Lewis acid sites.

There are many possibilities in the CB oxidation process, especially the hydrolysis reaction, which can easily transfer Cl and thus affect the chlorination of the active component on the catalyst. It was necessary to further investigate the Cl residue on the surface of spent catalysts. Cl 2p XPS analyses were conducted for the spent catalysts as shown in Fig. 6a. The Cl 2p spectra was deconvoluted into three groups of peaks. Normally, the B.E. of organic Cl species were relatively high, so the peaks at 198.7 eV ($2p_{3/2}$) and 200.3 eV ($2p_{1/2}$) was due to the organic Cl species (Cl_{or}). The bridging Cl atoms (Cl_{br}) presented at 198.1 eV and 199.7 eV, which came from the replacement of bridged O atoms on RuO_2 and PtO_x [37]. The peaks at 197.6 eV and 199.2 eV were assigned to the chemically adsorbed Cl atoms (Cl_{ad}). Among the different Cl species, Cl_{ad} was generally considered as active Cl species to form inorganic chlorine HCl, and Cl_{or} acted as the chlorinated organic skeletons for further chlorination, and Cl_{br} are due to the MO_xCl_y (i.e., RuO_xCl_y and PtO_xCl_y), which were stable and can deteriorate the oxidation capacity of Ru and Pt sites. As shown in Fig. 6a, during the CB oxidation process, Cl_{or} and Cl_{ad} species were dynamically balanced on the catalyst-surface and showed similarity in the Cl distributions. RuPt-ALD-spent showed the lowest Cl_{br} peak intensity, which might be the reason for its strongest endurance to MO_xCl_y formation and best stability.

As shown in Fig. 6b, the surface atomic molar ratio of $\text{Ru}^0/\text{Ru}^{4+}$ of RuPt-ALD changed from 0.44 to 1.35 after reaction. Clearly, when CB was feed in, the ratio of Ru^0 increased during the catalytic oxidation process, which was reported to be possibly owe to the reduction of organic compounds [52]. In addition, molecular adsorbed oxygen was easier to be activated on Ru^0 as the procedure of $\text{O}_2(\text{ad}) \rightarrow \text{O}_2^-(\text{ad}) \rightarrow \text{O}^-(\text{ad}) \rightarrow \text{O}^{2-}(\text{lattice})$, during the process Ru^0 lost electrons and transformed into Ru^{4+} . At the same time, Ru^{4+} was universally acknowledged as an active component for Cl species removal and deep oxidation of CB. The CB oxidation followed the Mars and van Krevelen (MvK) mechanism over RuPt-ALD. Lattice oxygen of Ru-O-Pt bonds was continuously consumed during the CB deep oxidation, which changed

the Ru^{4+} into Ru^0 . Subsequently, Ru^0 could activate molecular adsorbed oxygen and turn into Ru^{4+} . The plentiful active oxygen species produced during the changes in oxidation states of noble metals further promoted the desorption capacity of Cl species, and avoided the formation of RuO_xCl_y .

3.5. Role of water during the CB oxidation

In order to further explore the effect of water vapor on catalyst performance, we performed the CB oxidation reaction in the absence of water (dry gas, Fig. 7a) and compared with the condition of humid gas. Clearly, in the absence of water, CB conversion was obviously improved, the T_{50} and T_{90} of the samples were summarized in the Table 3. The T_{50} of Ru-IM decreased from 245 °C to 223 °C in dry gas and that of the Pt-IM catalyst decreased from 230 °C to 227 °C, while that of RuPt-ALD dropped from 176 °C to 143 °C. These results indicate that the presence of water vapor has a negative effect on the total conversion of CB. Notably, Ru-IM seems to have worse water resistance than Pt-contained samples. At the same temperature (200 °C), the reaction rate (1.98 mmol/(g h)) and TOF (1.78 h^{-1}) of Ru-IM under high humidity condition were only half of that under dry gas condition (4.03 mmol/(g h) and 3.63 h^{-1}). The reaction rate and TOF of Pt-IM dropped by about 35 % under the feed containing high content of water. RuPt-ALD sample has the strongest water resistance, the reaction rate and TOF of RuPt-ALD only decreased slightly (from 8.43 to 8.31 mmol/(g h), and from 4.58 to 4.52 h^{-1}) in the presence high content of water.

For the Ru-IM and Pt-IM samples, Cl_2 selectivity was significantly higher in the absence of water (Fig. 7b). This means that the addition of water makes the surface of the catalyst rich in hydroxyl groups. And the combination between Cl and surface hydroxyl group occurs easily to form HCl. By comparing the selectivity of Cl_2 and HCl under dry and wet feed, the removal of Cl was greatly improved in wet feed as HCl. This result shows that the Cl is more easily removed in the form of HCl in the wet feed, but not easily retained on the catalyst surface. In other words, the presence of water vapor plays a two-sided role in the CB oxidation reaction. On one hand, the poor catalytic activity in humid air can be attributed to the competitive adsorption of H_2O with CB and O_2 molecules, which inhibited the activation process of O_2 on the active sites. Oppositely, the presence of water facilitated the increase of Brønsted

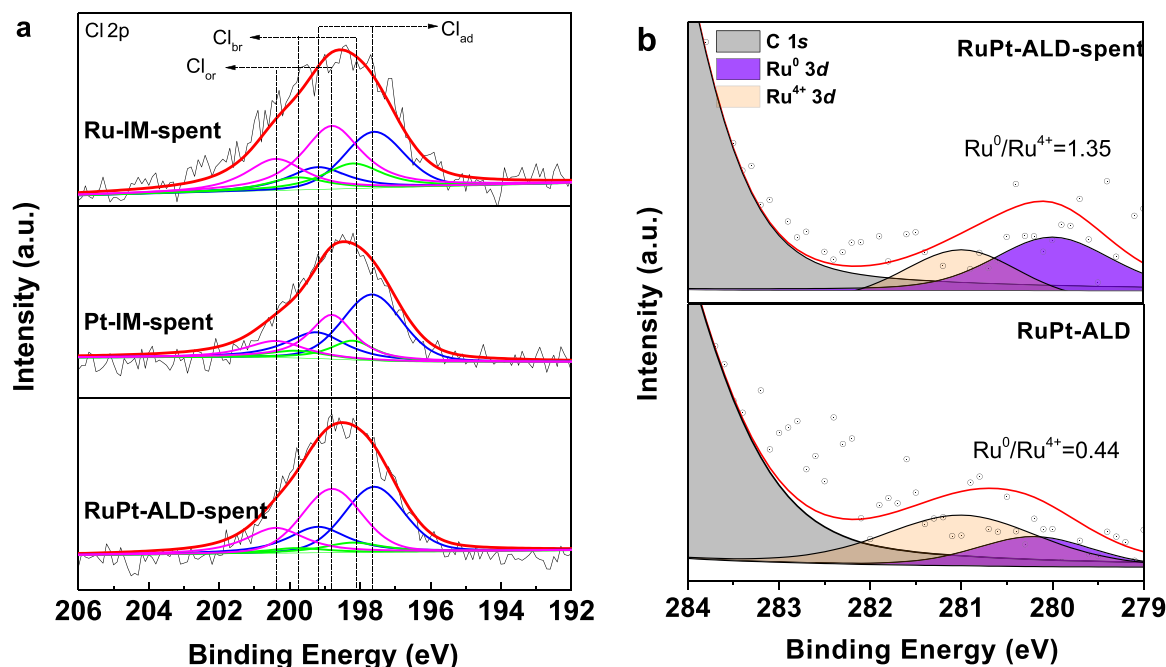


Fig. 6. (a) XPS spectra of Cl 2p of the spent Ru-IM, Pt-IM and RuPt-ALD catalysts. (b) XPS spectra of Ru 3d of the fresh and spent RuPt-ALD catalysts.

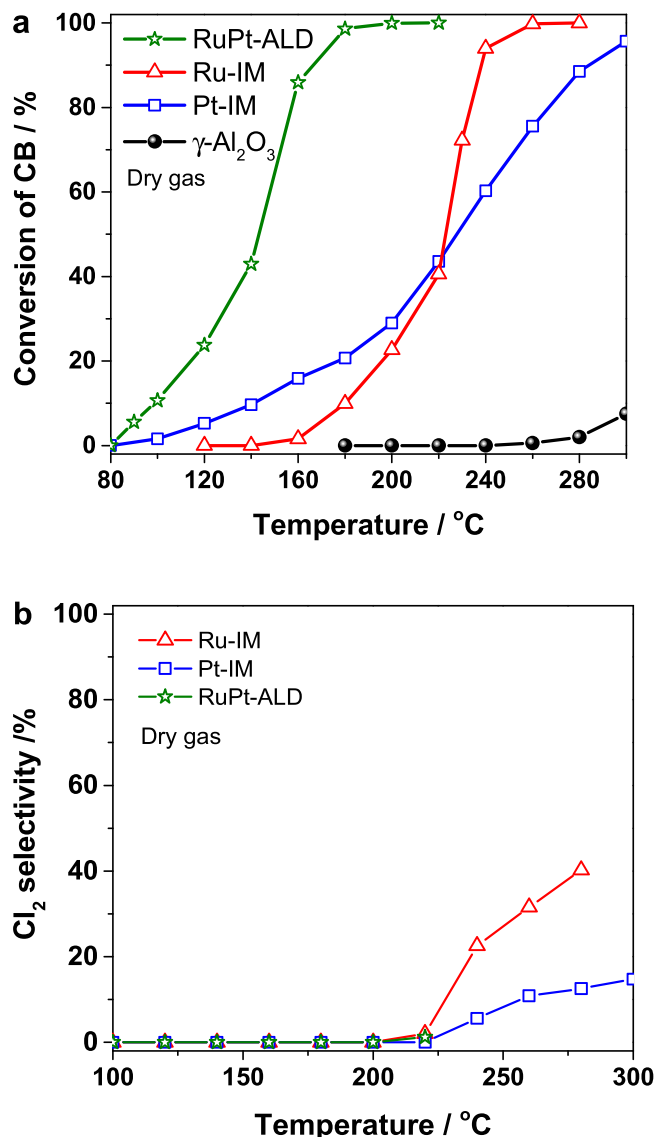


Fig. 7. (a) CB conversion as a function of temperature and (b) Cl₂ selectivity of Ru-IM, Pt-IM and RuPt-ALD catalysts in dry air. Reaction condition: 167 ppm CB/dry air, GHSV = 20,000 mL/g h, catalyst mass: 200 mg.

acid sites, which further promote the dechlorination reaction.

3.6. Density functional theory calculations

Density functional theory (DFT) calculations were employed to gain insight into the stronger CB adsorption and oxygen activation, and resistance to chlorine poisoning capacity of RuPt-ALD with Pt(111) and RuO₂(110) surface slabs. RuO₂(110) with different terminated configurations were studied as shown in Fig. S5, O^{top} termination with the presence of both twofold- and onefold- coordinated O^{br} and O^{top} atoms was considered to be the most stable under the experimental condition ($T = 200^\circ\text{C}$, $P_{\text{O}_2} = 0.2\text{atm}$). In Fig. S5b, the oxygen chemical potential μ_{O} was calculated as a function of temperature T and oxygen partial pressure $P = P_{\text{O}_2}$, with half of E_{O_2} calculated by VASP as zero reference [53]. The most stable termination was the one that minimized the surface energy, $\gamma(T, P)$, defined as

$$\gamma(T, P) = \frac{1}{2A} [G^{\text{slab}}(T, P, N_{\text{Ru}}, N_{\text{O}}) - N_{\text{Ru}} G_{\text{RuO}_2}^{\text{bulk}}(T, P) + (2N_{\text{Ru}} - N_{\text{O}}) \mu(\text{O})(T, P)] \quad (6)$$

where A was the area of the exposed termination of a single cell. Bulk and slab solid free energies G were taken from optimized DFT structures. N_{Ru} and N_{O} represented the number of Ru and O atoms in RuO₂ bulk unit cell. In our experiment condition, $\gamma(T = 200^\circ\text{C}, P_{\text{O}_2} = 0.2\text{atm})$ was calculated as -0.5 eV , which signified that the RuO₂(110)-O^{top} termination is the most stable. Besides, according to the calculated E_{O_v} in Fig. S5a, the O-top atoms were more likely to form oxygen vacancy (V_{O}) than O-br atoms. However, the formation of oxygen vacancy from two adjacent O-top atoms overcame higher barrier of 1.01 eV in Fig. S5c than O₂ dissociation barriers of other catalysts in Fig. 8, which indicated difficult O₂ activation at Ru-IM catalyst.

The as-synthesized RuPt-ALD catalyst was modeled as the RuO_x cluster decorated onto Pt(111) slab in the light of Fig. 2g and h. The stability of the supported Ru single atom, Ru_n clusters and (RuO₂)_n clusters was evaluated by calculating its binding energy E_{bind} , as defined in

$$E_{\text{bind}}(X) = \frac{1}{n} (E_{X+\text{slab}} - E_{\text{slab}} - n \cdot \frac{E_{\text{bulk}}}{N}) \quad (7)$$

where $E_{X+\text{slab}}$, E_{slab} , and E_{bulk} are the total energies of the X/Pt(111) slab, the bare Pt(111) slab, and a single Ru or RuO₂ bulk, respectively. N represents the number of Ru atoms or (RuO₂)₁ in Pt or RuO₂ unit cell. n corresponds to the number of Ru atoms or (RuO₂)₁ units contained in the adsorbate X. The smaller the value of E_{bind} indicates the more stable X/Pt(111) configuration. The (RuO₂)₃/Pt(111) is the most stable of all models considered in Fig. S6. The model Ru₃O₆/Pt(111) configuration indicated the effective anchor of RuO_x cluster on Pt(111) with charge transfer between Ru₃O₆ and Pt(111) shown in Fig. S7.

Fig. 8 compared the reaction paths and energy changes of oxygen activation and chlorine species desorption on the three catalysts, with configuration details shown in Table S2. O₂ preferred lying flat on Pt~Pt sites with an E_{ad} of -0.55 eV and dissociated directly with a modest barrier of 0.51 eV on Pt(111). In case of Ru₃O₆/Pt(111) interface, the adsorption of O₂ was moderately weakened and its decomposition overcame a low barrier of 0.19 eV with the assistance of Ru atom in Ru₃O₆ cluster. The energetic routes of O₂ dissociation at the sites adjacent to Ru₃O₆/Pt(111) interface were similar to clean Pt(111) slab as shown in Fig. S8a, suggesting the RuPt-ALD has the oxygen dissociation capacity similar to bare Pt. However, the weak physical adsorption on RuO₂(110)-O^{top} and large E_{O_v} of surface lattice oxygens led to relatively difficult O₂ activation. The effect of oxygen content on the reaction rate was tested in Fig. 9d (top), with changing O₂ concentration ([O₂]) from 1 % to 19.7 % in the feed containing 167 ppm CB, the CB reaction rate over RuPt-ALD increased gradually, while Ru-IM and Pt-IM presented low rates with slowly rising. This result indicated that the availability of surface oxygen on oxygen vacancies contacted with Ru-O-Pt interface is promoted by [O₂]. Since the whole procedure followed the Mars and van Krevelen mechanism, the noble metals that were reduced during the CB deep oxidation (i.e., Ru⁰ and Pt⁰) could bond oxygen faster and fuller at higher O₂ concentrations in gas phase. And play key roles in the activation of gas phase oxygen and the transition to oxidation states. Note that in catalytic oxidation of chlorinated VOCs, the role of oxygen besides acting as an oxidizing agent also includes resisting chlorine poisoning, forming a new active phase during reaction, and determining the distribution of products or by-products. Therefore, the influence of oxygen concentration on the oxidation process of chlorobenzene is complicated. The data in this work only investigated the effect on reaction rate, but not the influences on other aspects, which should be further studied.

On the other hand, the desorption paths of HCl and Cl₂ were calculated to evaluate the ability of chlorine desorption. The produced HCl* and Cl₂* species only needed potential barriers lower than 0.10 eV to desorb due to their weak adsorption in all cases. But the combination of adsorbed H and Cl atoms or two adsorbed Cl atoms overcame higher barriers of 0.60 eV or 2.27 eV on Pt(111) than that of RuO₂(110)-O^{top}

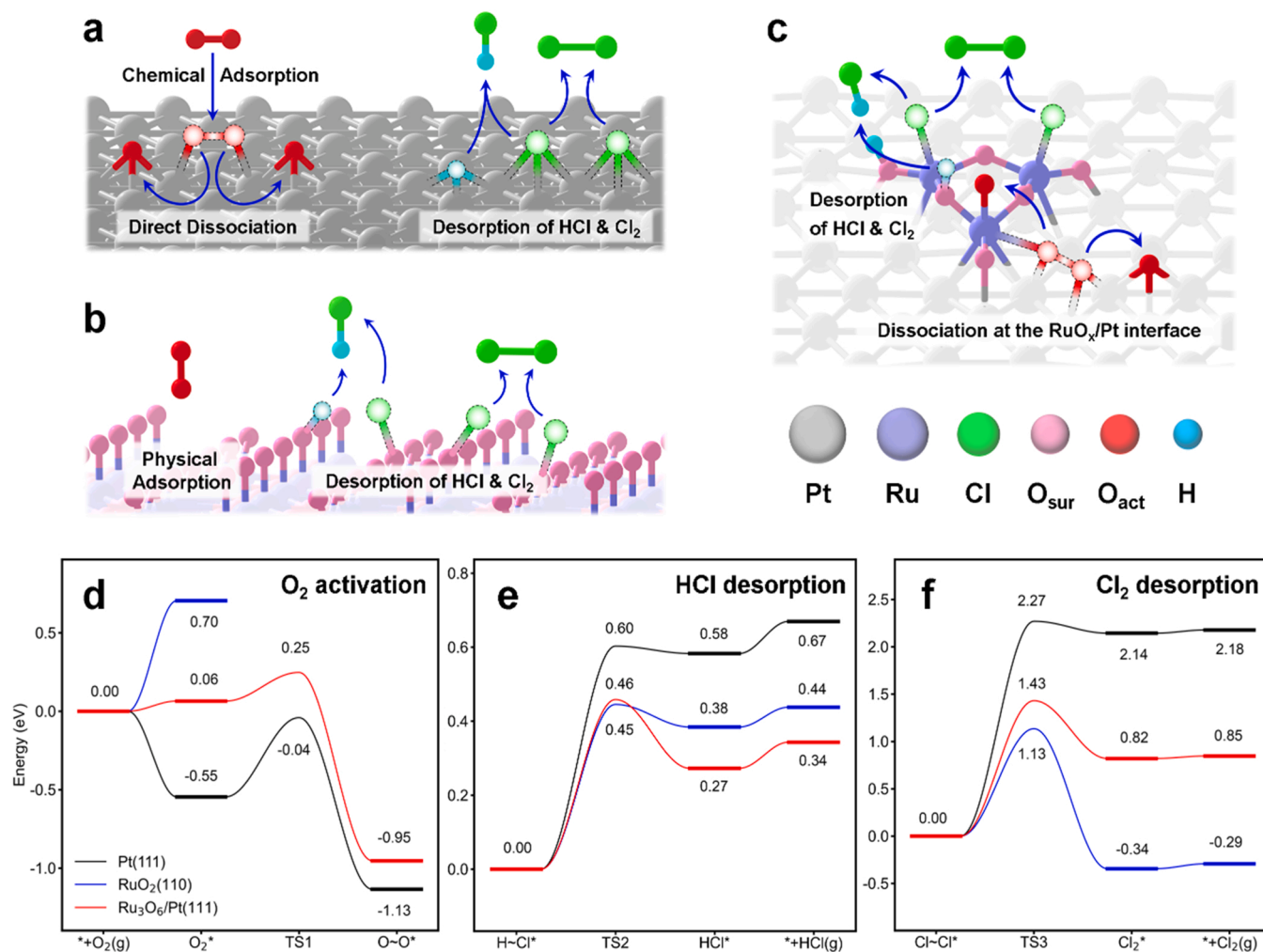


Fig. 8. Schematic diagrams of O_2 activation, HCl desorption and Cl_2 desorption of (a) Pt(111), (b) $RuO_2(110)-O^{top}$ and (c) $Ru_3O_6/Pt(111)$ and their corresponding energetic routes (d-f). The gray, purple, green and blue spheres represented Pt, Ru, Cl and H atoms, respectively; the pink and red spheres represented O atoms on the surface and from O_2 . The arrows indicated the reaction-proceeding directions, the intermediates with stars represented the adsorbates bonded to the active sites and wavy lines connected co-adsorbed species.

and $Ru_3O_6/Pt(111)$, which suggested that chlorine poisoning is more likely to occur on Pt(111). Although the energy barrier of Cl_2 desorption over $RuO_2(110)$ was lower than $Ru_3O_6/Pt(111)$ model, this result indicated that the addition of Ru on Pt NPs can promote Cl desorption ability, thus avoiding the accumulation of inorganic Cl on the catalyst. Note that although DFT calculation showed that the desorption ability of the three catalysts for Cl has a good correlation with their catalytic performance, the desorption ability of Cl under humid conditions may not be the most important factor. However, Cl desorption ability may be a key factor in dry feed conditions, according to their catalytic performance in dry feed as shown in Fig. 7a and Fig. 4a. The most obvious signal was that the catalytic performance of Pt-IM sample was greatly improved under wet feed, indicating that Pt-IM was more likely to accumulate Cl and be inactivated under dry gas feed, while the influence of Cl poisoning was greatly reduced by wet feed. Therefore, Pt-IM showed better catalytic activity in wet feed.

The adsorption capacity for CB was further investigated by DFT-D3 method with Becke-Jonson damping and the corresponding characteristic bonding features was further validated by determining the charge density difference plots shown in Fig. 9a to c. For the oxygen rich termination $RuO_2(110)-O^{top}$, CB preferred the bridge sites between O^{top} and O^{bri} atoms with an E_{ad} of -0.38 eV accompanied by electrons mainly transferred from the Cl atom of CB to the carrier. CB tended to be captured by forming the single covalent Pt-Cl bond on clean Pt(111)

surface and the corresponding E_{ad} was calculated to be -0.45 eV. Notably, with the $(RuO_2)_3$ clusters loaded, the Pt atoms adjacent to interface were activated by the increased electronic density, resulting in an increase of about 20 % according to the decreased value of ICOHP in Fig. S9 (More negative ICOHP means the stronger bond strength of Pt-Cl bond.), which is derived from more bonding and less anti-bonding COHP components of Pt-Cl bond of adsorbed CB on $Ru_3O_6/Pt(111)$. Moreover, there are also electrons transferred from the H atoms of CB to the O atoms of Ru-O-Pt bonds at the interface shown in Fig. 9c, which is further conducive to the adsorption of CB with binding strength 0.17 eV stronger than that of clean Pt(111) slab. In sum, the order of E_{ad} for these models were $RuPt-ALD$ (-0.62 eV) > $Pt-IM$ (-0.45 eV) > $Ru-IM$ (-0.38 eV), which is in good agreement with their catalytic activities shown in Fig. 4a. By comparing these processes (CB adsorption, oxygen activation and inorganic chlorine desorption), the relatively weak adsorption of CB molecules on the active sites was a slow step, indicating that it may be the rate-control step in the catalytic oxidation of CB. Then we studied the effect of different CB concentrations on the reaction rate at $200^\circ C$ over $RuPt-ALD$ sample in Fig. 9d (bottom). With increasing CB concentration from 167 to 1000 ppm in the feed containing 5 vol% H_2O/air , increase in rate over $RuPt-ALD$ was observed. This result suggested that the increase in CB adsorption was favorable for the reaction on $RuPt-ALD$. Overall, it can be deduced that $RuPt-ALD$ catalyst with plentiful Ru-O-Pt bonds has higher activity, due to the synergism

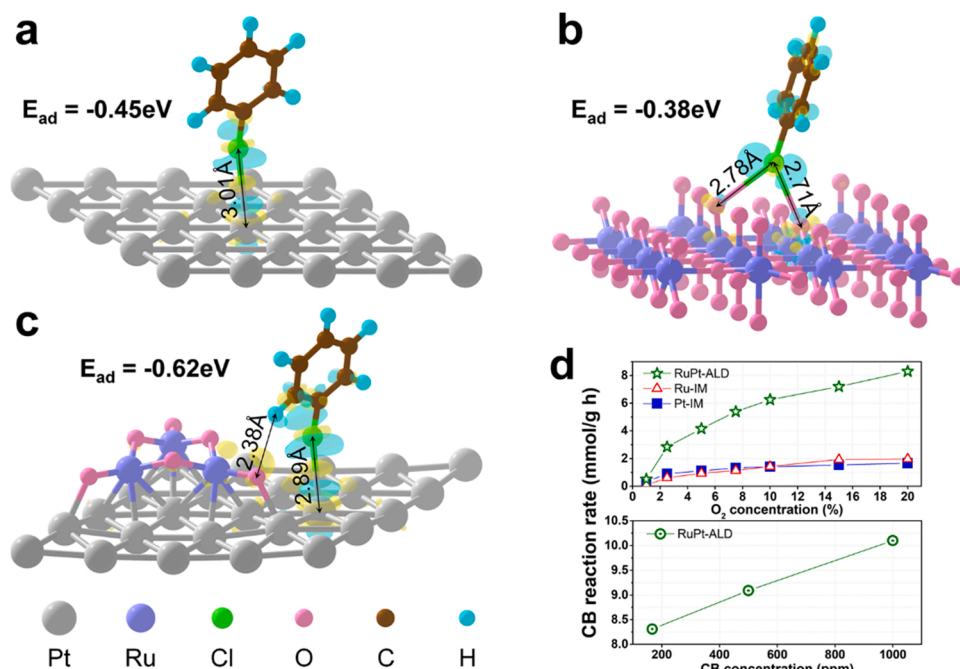


Fig. 9. The charge density difference between adsorbed CB and (a) Pt(111), (b) RuO₂(110)-O^{top} and (c) Ru₃O₆/Pt(111) with corresponding adsorption energies. The yellow and cyan represented positive and negative charges regions with 0.001 e bohr⁻³ isosurface level. (d) top, CB reaction rate at 200 °C vs. [O₂] over Ru-IM, Pt-IM and RuPt-ALD catalysts (167 ppm CB/5 vol % H₂O/1 %, 2.5 %, 5 %, 7.5 %, 10 %, 15 %, 19.7% O₂/N₂ balance); bottom, CB reaction rate at 200 °C vs. [CB] over RuPt-ALD catalyst (167, 500, 1000 ppm CB/5 vol% H₂O/19.7% O₂/N₂ balance).

between stronger CB adsorption capacity, the lower barriers of O₂ dissociation, and the removal of Cl species.

3.7. Structure-activity relationships

It is well known that the catalytic oxidation of VOCs is an exothermic reaction and there are several factors playing roles in VOCs oxidation, such as the mass transfer rate, the adsorption capacity of the reactant on the catalyst surface, and the surface properties of catalysts (including surface area, pore structure, particle size, oxidation state of precious metals, properties of interfaces between bimetals, adsorbed/lattice oxygen species, oxygen vacancy, redox properties, acid sites, etc). Generally, there were four facts should be concerned for catalytic oxidation of CB in this work. Firstly, the adsorption of reactants, including oxygen, CB, and possibly water on catalyst surface, was the first step for CB oxidation, since catalytic oxidation of VOCs always runs in diffusion regime, where the reaction rate was limited by the mass transfer between catalyst and flowing gas mixture. This, in turn, depended on the adsorption capacity of the active component of the catalyst to the reactant. Herein, the adsorption capacity of CB have been simulated by DFT method and studied by experiment, shown in Fig. 9. The Ru-Pt atoms adjacent to interface were activated by the increased electronic density, and there are also electrons transferred from the H atoms of CB to the O atoms of Ru-O-Pt bonds at the interface. The adsorption process of the reactant CB was promoted by the synergism between the Ru-Pt components, and this process at the catalytic active interface is the rate-determining step for the catalytic oxidation of CB in the current catalytic system.

Secondly, the dechlorination reaction was normally the second step for CB oxidation. The acidity of the catalysts was reported to play vital roles in the dichlorination reaction [15,34]. The electron-withdrawing effect of Lewis acids can weaken the conjugation effect between the C-Cl bond, which promotes the dechlorination reaction at lower temperature. As for the surface acidity of the catalysts, NH₃-TPD result indicated that the coordinatively unsaturated Pt and Ru atoms had an electron-accepting ability to adsorb ammonia molecules, which created new Lewis acid sites. As the NH₃-TPD result suggested the incorporation of Ru and Pt could promote the formation of Lewis acid on the catalyst surface, RuPt-ALD catalyst with abundant medium acids and stronger

Lewis and Brønsted acidity were responsible to perform better in CB oxidation.

Thirdly, the third step of CB oxidation is often the deep oxidation of benzene after dechlorination. Thus, the redox capacity of the catalyst plays a very important role in this step. It is known that the active oxygen species consumed with benzene, and gaseous O₂ molecules subsequently replenished the consumed surface oxygen species on active sites. However, the latest research showed that higher redox capacity is not always better for CVOs oxidation [2]. Normally, catalysts with strong redox properties promoted Cl₂ formation by semi-Deacon reaction ($2\text{Cl}^- + \text{O}_2 + \text{V}_o = \text{Cl}_2 + 2\text{O}_{\text{lat}}$), thus chlorination into organic byproducts, and deposition on catalyst surface. Therefore, rational modification of catalysts with appropriate redox property to improve further oxidation of intermediates at lower temperature will prevent the possibility of Cl₂ and polychlorinated byproducts formation. As for the redox capacity of the catalysts, H₂-TPR result indicated that RuPt-ALD catalyst could eliminate the bulk RuO₂ species and enable the formation of Ru clusters with uniform dispersion on the Pt/Al₂O₃. H₂-TPR and DFT calculation implied the oxygen activation capacity of RuPt-ALD catalyst was not as strong as bare Pt sample, due to the strong interaction between Ru and Pt species. As a result, RuPt-ALD with appropriate redox property and enhancing acidic sites were feasible to alleviate chlorination that inhibited chlorinated byproducts formation. The distribution of DCB by-products presented in Fig. 4d and Cl₂ selectivity presented in Fig. 7b and S4b has confirmed this advantage.

Finally, the deactivation of catalyst is always unavoidable due to the strong adsorption of the dissociated Cl species on active sites. An efficient catalyst for CVOs oxidation should possess plenty of acids sites, appropriate redox property and great resistance to chlorine poisoning. As for the ability of chlorine desorption, we found the Cl is more easily removed in the form of HCl in the wet feed, and not easily retained on the catalyst surface. But in dry feed, the combination of adsorbed H and Cl atoms or two adsorbed Cl atoms overcame higher barriers of 0.60 eV or 2.27 eV on Pt model than that of Ru or RuPt models, which suggested that chlorine poisoning is more likely to occur on Pt-based catalysts. Therefore, we believed that there were two main factors contributing to the catalytic performance of RuPt-ALD under wet feed. One was the stronger CB adsorption capacity, which was also the rate-determining step in the catalytic oxidation of CB. Another one was the appropriate

O₂ activation ability, which was verified by H₂-TPR, the experiment of effect of oxygen content on reaction rate, and DFT calculations. Under dry feed conditions, in addition to the above two factors, the catalytic performance of Pt-based catalysts is also influenced by the desorption ability of Cl, as mentioned in DFT calculation.

4. Conclusions

This work successfully designed and fabricated Ru-Pt bimetallic elements on γ -Al₂O₃ by the selective ALD route. The obtained RuPt-ALD catalyst showed remarkably improved activity ($T_{50} = 176$ °C and $T_{90} = 196$ °C) and brilliant stability in CB catalytic oxidation. Both experimental and theoretical studies indicated that the RuPt complex contained Ru-Pt bonding and Ru is firmly anchored on Pt(111) surface through charge transfer. The strong interaction between Pt and Ru and the formation of Ru-O-Pt bond at the interface could enhance Lewis acid and inhibit the accumulations of Cl, which further observably suppressed the formation of polychlorinated by-products. The appropriate redox property and acidity were also favorable for reducing coke on catalyst surface and promoting stability. It was then confirmed the RuPt-ALD sample was superior in the processes of reactants (CB and O₂) adsorption and activation, which played crucial roles in the oxidation of CB in wet feed. RuPt-ALD was also easier to desorption of Cl-contained products (HCl and Cl₂), guaranteeing it more advantageous in dry feed conditions. This work exemplifies ALD as a useful tool in the development of superior bimetallic catalysts that can be used to improve CVOs oxidation and meet increasingly stringent emission targets.

CRediT authorship contribution statement

Yu Wang, investigation, writing - original draft. **Chun Du**, writing - original draft. **Zhang Liu**, writing - review & editing. **Yanfei Liu**, writing - original draft. **Rong Chen** resources. **Bin Shan** and **Limin Guo**, supervision, project administration, resources, review & editing.

Declaration of Competing Interest

The authors declare that they have no known competing financial interests or personal relationships that could have appeared to influence the work reported in this paper.

Data availability

Data will be made available on request.

Acknowledgments

The present work is supported by the National Natural Science Foundation of China (21906125, 52171209), a program for the HUST Academic Frontier Youth Team (2018QYTD03), Natural Science Foundation of Hubei Province (2019CFA070), and Key R&D Program of Hubei Province (2021BCD002). The authors thank the Analysis and Testing Center of Huazhong University of Science and Technology, the Analysis and Testing Center of Wuhan University of Science and Technology for analytical support.

Appendix A. Supporting information

Supplementary data associated with this article can be found in the online version at [doi:10.1016/j.apcatb.2023.122648](https://doi.org/10.1016/j.apcatb.2023.122648).

References

- [1] F. Lin, L. Xiang, Z. Zhang, N. Li, B. Yan, C. He, Z. Hao, G. Chen, Comprehensive review on catalytic degradation of Cl-VOCs under the practical application conditions, *Crit. Rev. Environ. Sci. Technol.* 52 (2020) 311–355.
- [2] F. Lin, Z. Zhang, N. Li, B. Yan, C. He, Z. Hao, G. Chen, How to achieve complete elimination of Cl-VOCs: a critical review on byproducts formation and inhibition strategies during catalytic oxidation, *Chem. Eng. J.* 404 (2021), 126534.
- [3] M.A. Salae, A.A. Salae, T.S. Kharlamova, G.V. Mamontov, Pt-CeO₂-based composites in environmental catalysis: a review, *Appl. Catal. B: Environ.* 295 (2021), 120286.
- [4] Y. Guo, M. Wen, S. Song, Q. Liu, G. Li, T. An, Enhanced catalytic elimination of typical VOCs over ZnCoOx catalyst derived from in situ pyrolysis of ZnCo bimetallic zeolitic imidazolate frameworks, *Appl. Catal. B: Environ.* 308 (2022), 121212.
- [5] H. Zhang, X. Gao, B. Gong, S. Shao, C. Tu, J. Pan, Y. Wang, Q. Dai, Y. Guo, X. Wang, Catalytic combustion of CVOs over MoOx/CeO₂ catalysts, *Appl. Catal. B: Environ.* 310 (2022), 121240.
- [6] X. Lv, M. Jiang, J. Chen, D. Yan, H. Jia, Unveiling the lead resistance mechanism and interface regulation strategy of Ru-based catalyst during chlorinated VOCs oxidation, *Appl. Catal. B: Environ.* 315 (2022), 121592.
- [7] Y. Wang, Y. Chen, L. Zhang, G. Wang, W. Deng, L. Guo, Total catalytic oxidation of chlorinated aromatics over bimetallic Pt–Ru supported on hierarchical HZSM-5 zeolite, *Microporous Mesoporous Mater.* 308 (2020), 110538.
- [8] W. Yu, M.D. Porosoff, J.G. Chen, Review of Pt-based bimetallic catalysis: from model surfaces to supported catalysts, *Chem. Rev.* 112 (2012) 5780–5817.
- [9] C. Huang, H. Liu, Y. Tang, Q. Lu, S. Chu, X. Liu, B. Shan, R. Chen, Constructing uniform Sub-3 nm PtZn intermetallic nanocrystals via atomic layer deposition for fuel cell oxygen reduction, *Appl. Catal. B: Environ.* (2022), 121986.
- [10] X. Liu, S. Jia, M. Yang, Y. Tang, Y. Wen, S. Chu, J. Wang, B. Shan, R. Chen, Activation of subnanometric Pt on Cu-modified CeO₂ via redox-coupled atomic layer deposition for CO oxidation, *Nat. Commun.* 11 (2020) 4240.
- [11] W.W. McNeary, S.A. Tacey, G.D. Lahti, D.R. Conklin, K.A. Unocic, E.C.D. Tan, E. C. Wegener, T.E. Erden, S. Moulton, C. Gump, J. Burger, M.B. Griffin, C. A. Farberow, M.J. Watson, L. Tuxworth, K.M. Van Allsburg, A.A. Dameron, K. Buechler, D.R. Vardon, Atomic layer deposition with TiO₂ for enhanced reactivity and stability of aromatic hydrogenation catalysts, *ACS Catal.* 11 (2021) 8538–8549.
- [12] Y. Kim, S. Xu, J. Park, A.L. Dadlani, O. Vinogradova, D. Krishnamurthy, M. Orazov, D.U. Lee, S. Dull, P. Schindler, H.S. Han, Z. Wang, T. Graf, T.D. Schladt, J. E. Mueller, R. Sarangi, R. Davis, V. Viswanathan, T.F. Jaramillo, D.C. Higgins, F. B. Prinz, Improving intrinsic oxygen reduction activity and stability: atomic layer deposition preparation of platinum-titanium alloy catalysts, *Appl. Catal. B: Environ.* 300 (2022), 120741.
- [13] X. Du, Y. Lang, K. Cao, J. Yang, J. Cai, B. Shan, R. Chen, Bifunctionally faceted Pt/Ru nanoparticles for preferential oxidation of CO in H₂, *J. Catal.* 396 (2021) 148–156.
- [14] L. Zhang, R. Si, H. Liu, N. Chen, Q. Wang, K. Adair, Z. Wang, J. Chen, Z. Song, J. Li, M.N. Banis, R. Li, T.K. Sham, M. Gu, L.M. Liu, G.A. Botton, X. Sun, Atomic layer deposited Pt-Ru dual-metal dimers and identifying their active sites for hydrogen evolution reaction, *Nat. Commun.* 10 (2019) 4936.
- [15] Y. Wang, X. Wang, J. Gong, X. Fan, Z. Zhou, Improved chlorobenzene oxidation over Fe-Mn oxide by Ni doping: the effect of oxidative ability and surface acidity, *Appl. Catal. A: Gen.* 644 (2022), 118809.
- [16] Z. Abbasi, M. Haghighi, E. Fatehifar, S. Saedy, Synthesis and physicochemical characterizations of nanostructured Pt/Al₂O₃-CeO₂ catalysts for total oxidation of VOCs, *J. Hazard. Mater.* 186 (2011) 1445–1454.
- [17] W. Liu, S. Yang, Q. Zhang, T. He, Y. Luo, J. Tao, D. Wu, H. Peng, Insights into flower-like Al₂O₃ spheres with rich unsaturated pentacoordinate Al³⁺ sites stabilizing Ru-CeOx for propane total oxidation, *Appl. Catal. B: Environ.* 292 (2021), 120171.
- [18] N.A. Roslan, S. Zainal Abidin, O.U. Osazuwa, S.Y. Chin, Y.H. Taufiq-Yap, Enhanced syngas production from glycerol dry reforming over Ru promoted -Ni catalyst supported on extracted Al₂O₃, *Fuel* 314 (2022), 123050.
- [19] Y. Park, H. Ku, J.-Y. An, J. Han, C.-H. Shin, J.-K. Jeon, Effect of MgO promoter on Ru/ γ -Al₂O₃ catalysts for tricyclopentadiene hydrogenation, *Catal. Today* 352 (2020) 308–315.
- [20] S.-Y. Chen, C.-L. Chang, M. Nishi, W.-C. Hsiao, Y.I.A. Reyes, H. Tateno, H.-H. Chou, C.-M. Yang, H.-Y.T. Chen, T. Mochizuki, H. Takagi, T. Nanba, Unraveling the active sites of Cs-promoted Ru/ γ -Al₂O₃ catalysts for ammonia synthesis, *Appl. Catal. B: Environ.* 310 (2022), 121269.
- [21] R. Liu, S. Liu, H. Ding, D. Zhao, J. Fu, Y. Zhang, W. Huo, G.K. Li, Unveiling the Role of Atomically Dispersed Active Sites over Amorphous Iron Oxide Supported Pt Catalysts for Complete Catalytic Ozonation of Toluene at Low Temperature, *Ind. Eng. Chem. Res.* 60 (2021) 3881–3892.
- [22] E. Gonzalez-A, R. Rangel, A. Solís-García, A.M. Venezia, T.A. Zepeda, FTIR investigation under reaction conditions during CO oxidation over Ru(x)-CeO₂ catalysts, *Mol. Catal.* 493 (2020), 111086.
- [23] C. Li, L. Zhang, Y. Zhang, Y. Zhou, J. Sun, X. Ouyang, X. Wang, J. Zhu, Y. Fu, PtRu alloy nanoparticles embedded on C₂N nanosheets for efficient hydrogen evolution reaction in both acidic and alkaline solutions, *Chem. Eng. J.* 428 (2022), 131085.
- [24] J. Serranoriz, G. Huber, M. Sanchezcastillo, J. Dumesic, F. Rodriguezreinoso, A. Sepulvedaescibano, Effect of Sn addition to Pt/CeO₂-Al₂O₃ and Pt/Al₂O₃ catalysts: an XPS, 119Sn Mössbauer and microcalorimetry study, *J. Catal.* 241 (2006) 378–388.
- [25] C.E. Finke, S.T. Omelchenko, J.T. Jasper, M.F. Lichterman, C.G. Read, N.S. Lewis, M.R. Hoffmann, Enhancing the activity of oxygen-evolution and chlorine-evolution electrocatalysts by atomic layer deposition of TiO₂, *Energy Environ. Sci.* 12 (2019) 358–365.

- [26] F. Wang, G. He, B. Zhang, M. Chen, X. Chen, C. Zhang, H. He, Insights into the activation effect of H₂ pretreatment on Ag/Al₂O₃ catalyst for the selective oxidation of ammonia, *ACS Catal.* 9 (2019) 1437–1445.
- [27] Y. Wang, S. Yao, M. Crocker, X. Zhu, B. Chen, J. Xie, C. Shi, D. Ma, An energy-efficient catalytic process for the tandem removal of formaldehyde and benzene by metal/HZSM-5 catalysts, *Catal. Sci. Technol.* 5 (2015) 4968–4972.
- [28] Y. Wang, D. Yang, S. Li, M. Chen, L. Guo, J. Zhou, Ru/hierarchical HZSM-5 zeolite as efficient bi-functional adsorbent/catalyst for bulky aromatic VOCs elimination, *Microporous Mesoporous Mater.* 258 (2018) 17–25.
- [29] A.-C. Johansson, J.V. Larsen, M.A. Verheijen, K.B. Haugshøj, H.F. Clausen, W.M. M. Kessels, L.H. Christensen, E.V. Thomsen, Electrocatalytic activity of atomic layer deposited Pt–Ru catalysts onto N-doped carbon nanotubes, *J. Catal.* 311 (2014) 481–486.
- [30] D. Teschner, R. Farra, L. Yao, R. Schlögl, H. Soerijanto, R. Schomäcker, T. Schmidt, L. Szentmiklósi, A.P. Amrute, C. Mondelli, J. Pérez-Ramírez, G. Novell-Leruth, N. López, An integrated approach to Deacon chemistry on RuO₂-based catalysts, *J. Catal.* 285 (2012) 273–284.
- [31] J. Pei, B. Peng, H. Lin, W. Chen, Y. Wang, J. Dong, J. Mao, D. Jia, W. Zhu, Z. Zhuang, Single-atom Ru on Al₂O₃ for highly active and selective 1,2-dichloroethane catalytic degradation, *ACS Appl. Mater. Interfaces* 13 (2021) 53683–53690.
- [32] M. Kourtelesis, X. Verykios, Stability of Pt/ γ -Al₂O₃ catalyst for the low temperature steam reforming of ethanol & acetaldehyde. Effect of carrier modification with Ca, *Mater. Today.: Proc.* 5 (2018) 27406–27415.
- [33] N.M. Kinnunen, J.T. Hirvi, M. Suvanto, T.A. Pakkanen, Methane combustion activity of Pd–PdOx–Pt/Al₂O₃ catalyst: the role of platinum promoter, *J. Mol. Catal. A: Chem.* 356 (2012) 20–28.
- [34] H. Liu, X. Li, Q. Dai, H. Zhao, G. Chai, Y. Guo, Y. Guo, L. Wang, W. Zhan, Catalytic oxidation of chlorinated volatile organic compounds over Mn–Ti composite oxides catalysts: elucidating the influence of surface acidity, *Appl. Catal. B: Environ.* 282 (2021), 119577.
- [35] W. Deng, Z. Jia, B. Gao, S. Zhu, D. Liu, L. Guo, Effect of preparation method on the performance of porous RuOx/Co₃O₄ catalysts for 1, 2-dichloroethane oxidation, *Appl. Catal. A: Gen.* 624 (2021), 118300.
- [36] X. Zhang, L. Dai, Y. Liu, J. Deng, L. Jing, X. Yu, Z. Han, K. Zhang, H. Dai, 3DOM CeO₂-supported Ru/M (M = Au, Pd, Pt) alloy nanoparticles with improved catalytic activity and chlorine-tolerance in trichloroethylene oxidation, *Catal. Sci. Technol.* 10 (2020) 3755–3770.
- [37] X. Liu, L. Chen, T. Zhu, R. Ning, Catalytic oxidation of chlorobenzene over noble metals (Pd, Pt, Ru, Rh) and the distributions of polychlorinated by-products, *J. Hazard. Mater.* 363 (2019) 90–98.
- [38] Q. Dai, S. Bai, J. Wang, M. Li, X. Wang, G. Lu, The effect of TiO₂ doping on catalytic performances of Ru/CeO₂ catalysts during catalytic combustion of chlorobenzene, *Appl. Catal. B: Environ.* 142–143 (2013) 222–233.
- [39] W. Pei, L. Dai, Y. Liu, J. Deng, L. Jing, K. Zhang, Z. Hou, Z. Han, A. Rastegarpanah, H. Dai, PtRu nanoparticles partially embedded in the 3DOM Ce_{0.7}Zr_{0.3}O₂ skeleton: active and stable catalysts for toluene combustion, *J. Catal.* 385 (2020) 274–288.
- [40] J. Zhao, W. Xi, C. Tu, Q. Dai, X. Wang, Catalytic oxidation of chlorinated VOCs over Ru/Ti_{0.9}Sn_{1-x} catalysts, *Appl. Catal. B: Environ.* 263 (2020), 118237.
- [41] J. Wang, H. Zhao, X. Liu, W. Xu, Y. Guo, J. Song, T. Zhu, Study on the catalytic properties of Ru/TiO₂ catalysts for the catalytic oxidation of (chloro)-aromatics, *Catal. Lett.* 149 (2019) 2004–2014.
- [42] Q. Dai, S. Bai, X. Wang, G. Lu, Catalytic combustion of chlorobenzene over Ru-doped ceria catalysts: mechanism study, *Appl. Catal. B: Environ.* 129 (2013) 580–588.
- [43] P. Topka, R. Delaigle, L. Kaluza, E.M. Gaigneaux, Performance of platinum and gold catalysts supported on ceria–zirconia mixed oxide in the oxidation of chlorobenzene, *Catal. Today* 253 (2015) 172–177.
- [44] R.W. van den Brink, R. Louw, P. Mulder, Formation of polychlorinated benzenes during the catalytic combustion of chlorobenzene using a Pt/ γ -Al₂O₃ catalyst, *Appl. Catal. B: Environ.* 16 (1998) 219–226.
- [45] Y. Wang, K. Liu, J. Wu, Z. Hu, L. Huang, J. Zhou, T. Ishihara, L. Guo, Unveiling the effects of alkali metal ions intercalated in layered MnO₂ for formaldehyde catalytic oxidation, *ACS Catal.* 10 (2020) 10021–10031.
- [46] Y. Wang, J. Wu, G. Wang, D. Yang, T. Ishihara, L. Guo, Oxygen vacancy engineering in Fe doped akhtenskite-type MnO₂ for low-temperature toluene oxidation, *Appl. Catal. B: Environ.* 285 (2021), 119873.
- [47] S. Cao, X. Fei, Y. Wen, Z. Sun, H. Wang, Z. Wu, Bimodal mesoporous TiO₂ supported Pt, Pd and Ru catalysts and their catalytic performance and deactivation mechanism for catalytic combustion of Dichloromethane (CH₂Cl₂), *Appl. Catal. A: Gen.* 550 (2018) 20–27.
- [48] Y. Gu, S. Shao, W. Sun, H. Xia, X. Gao, Q. Dai, W. Zhan, X. Wang, The oxidation of chlorinated organic compounds over W-modified Pt/CeO₂ catalysts, *J. Catal.* 380 (2019) 375–386.
- [49] G. Wang, Y. Wang, L. Qin, B. Zhao, L. Guo, J. Han, Efficient and stable degradation of chlorobenzene over a porous iron–manganese oxide supported ruthenium catalyst, *Catal. Sci. Technol.* 10 (2020) 7203–7216.
- [50] K. Shen, B. Gao, H. Xia, W. Deng, J. Yan, X. Guo, Y. Guo, X. Wang, W. Zhan, Q. Dai, Oxy-anionic doping: a new strategy for improving selectivity of Ru/CeO₂ with synergetic versatility and thermal stability for catalytic oxidation of chlorinated volatile organic compounds, *Environ. Sci. Technol.* 56 (2022) 8854–8863.
- [51] Y. Sun, S. Xu, B. Bai, L. Li, Y. Kang, X. Hu, Z. Liao, C. He, Biotemplate fabrication of hollow tubular CexSr_{1-x}TiO₃ with regulable surface acidity and oxygen mobility for efficient destruction of chlorobenzene: intrinsic synergy effect and reaction mechanism, *Environ. Sci. Technol.* 56 (2022) 5796–5807.
- [52] B. Sun, Q. Li, G. Su, B. Meng, M. Wu, Q. Zhang, J. Meng, B. Shi, Insights into chlorobenzene catalytic oxidation over noble metal loading 001-TiO₂(2): The role of NaBH₄ and subnanometer Ru undergoing stable Ru(0) <-> Ru(4+) circulation, *Environ. Sci. Technol.* 56 (2022) 16292–16302.
- [53] K. Reuter, M. Scheffler, Oxide formation at the surface of late 4d transition metals: insights from first-principles atomistic thermodynamics, *Appl. Phys. A* 78 (2004) 793–798.